FRANCESCA ESTELLE SIMONS

IMPROVING DREDGING PLUME PREDICTION MODELS USING SATELLITE IMAGERY

UNIVERSIDADE DO ALGARVE

Faculdade de Ciências e Tecnologia

2024

FRANCESCA ESTELLE SIMONS

IMPROVING DREDGING PLUME PREDICTION MODELS USING SATELLITE IMAGERY

Masters in Marine and Coastal Systems

Preformed under the supervision of:

Tim van der Biezen

Óscar Ferreira

UNIVERSIDADE DO ALGARVE

Faculdade de Ciências e Tecnologia

2024

Declaração de autoria de trabalho

Declaration of Authorship of work

IMPROVING DREDGING PLUME PREDICTION MODELS USING SATELLITE IMAGERY

Declaro ser o autor deste trabalho, que é original e inédito. Autores e trabalhos consultados estão devidamente citados no texto e constam da listagem de referências incluída.

I declare I am the author of this work, which is original and unpublished. The sources consulted have been duly cited in the text and included in the list of references.

Francesca Estelle Simons

Faro, 30 September 2024

First edition September 2024
This paper was published as *a dissertation requirement for the Master of Science degree in Marine and Coastal Systems.*

ACKNOWLEDGEMENT

The completion of this dissertation would not have been possible without the unwavering support of the following individuals:

The author would like to express gratitude to Óscar Ferreira, Tim van der Biezen, and Jeanine Vonkeman for their guidance, support, and patience in assisting with the progress of this dissertation.

Secondly, the author would like to express deep appreciation to all those who assisted in the realization of this dissertation. In particular, the author would like to thank the Boskalis Design, Tendering, and Engineering Department for their invaluable assistance in completing this thesis and for enabling the author to undertake the research at Boskalis.

Enorm bedankt, het ken net!

RESUMO

A indústria de dragagens é essencial para ganhar terrenos ao mar (aterros), proteção costeira, navegação e recuperação ambiental. No entanto, as actividades de dragagem produzem plumas de sedimentos em suspensão, que podem ter impactos económicos, sociais e ambientais significativos. Diferentes tipos de dragas, incluindo as dragas de sucção e arrasto (TSHD), geram estas plumas, que consistem em partículas finas suspensas na coluna de água. Estas plumas afectam os ecossistemas locais ao reduzirem a disponibilidade de luz e os níveis de oxigénio, prejudicando, por exemplo, as ervas marinhas e os corais. Consequentemente, são realizados Estudos de Impacto Ambiental (EIA) para analisar os potenciais impactos e garantir o cumprimento dos regulamentos.

Os modelos de transporte de sedimentos a grande distância são utilizados para estimar os Sólidos Suspensos Totais (TSS) como um indicador da turbidez. No entanto, estes modelos possuem incertezas devido ao reduzido conhecimento das características dos sedimentos e à complexidade dos processos de desenvolvimento da pluma. Um dos fatores de incerteza é o termo fonte, que representa o fluxo de sedimentos libertados durante a dragagem e é difícil de estimar com exatidão. O método de Becker, que envolve cálculos empíricos, é normalmente utilizado, mas introduz incertezas.

O transporte de sedimentos em plumas de dragagem é classificado em fases dinâmicas de campo próximo e fases passivas de campo distante. O campo próximo dinâmico é influenciado pela densidade e pelas interações dos navios, enquanto o campo distante passivo é regido pela hidrodinâmica ambiente. Uma modelação precisa requer abordagens separadas para os processos de campo próximo e de campo distante. Os modelos de campo distante, como o Delft3D e o MIKE, utilizam simulações em grande escala para prever a dispersão de sedimentos, mas os desafios incluem a estimativa de termos de origem, factores de dispersão e velocidades de sedimentação.

As imagens de satélite podem melhorar a modelação das plumas de sedimentos, fornecendo dados em tempo real sobre as extensões das plumas. O algoritmo do WaterInsight para imagens Sentinel-2 determina as concentrações de TSS, ajudando na calibração de modelos de sedimentos. Um ciclo de feedback compara as previsões do modelo com as observações de satélite, melhorando a precisão do modelo durante as fases de planeamento e execução. Nesse sentido, a Boskalis pretende reforçar o seu conjunto de ferramentas para a gestão de plumas de dragagem através da incorporação de dados de satélite.

Esta dissertação visou melhorar a seleção de parâmetros de dispersão de sedimentos para modelos Delft3D utilizando as técnicas de AbuShanab (2022) e Boersma (2023). Os principais objectivos incluiram:

- Definir o termo fonte, o fator de dispersão e os pressupostos de velocidade de sedimentação.
- Melhorar as definições dos parâmetros com base na análise de imagens de satélite.
- Avaliar a exatidão e a melhoria do modelo.
- Criar um ciclo de feedback para o aperfeiçoamento contínuo do modelo.

Este estudo demonstrou que as imagens de satélite podem ajudar a melhorar a exatidão dos modelos de transporte de sedimentos. O modelo que seria simulado na fase de planeamento e conceção (modelo PD) apresentou incertezas elevadas nas concentrações de TSS e na % de extensão da pluma em comparação com o modelo baseado em satélite (modelo SB). As imagens de satélite são utilizadas para analisar o comportamento da pluma, determinar os valores de concentração de fundo, os valores máximos de concentração e distinguir os navios apresentados nas imagens com a ajuda adicional dos trajectos dos navios AIS. Com esta informação e a utilização de ficheiros de registo, quando disponíveis, a informação adicional das imagens de satélite é utilizada para calibrar o modelo SB. Criação de gráficos de perfil ao longo dos trajectos dos navios AIS, gráficos de diferença e parâmetros de análise como RMSE, R2, viés e cálculos da % de extensão da pluma.

O modelo SB diferiu do modelo PD no valor de excedência de 80% do termo de fonte do pico de transbordo (P80), no posicionamento da pluma, na distribuição da fração IM e no fator de dispersão. O valor P80 foi inferior ao valor previsto e foi definido para ser libertado ao longo do trajeto do navio AIS a cada minuto relativamente ao termo de fonte estacionária do modelo PD. As fracções IM do modelo SB foram IM1 33% IM2 66% enquanto que o modelo PD teve IM1 66% e IM2 33% e o fator de dispersão foi fixado em 3 m2/s em vez de 1 m2/s.

Embora o modelo SB já seja mais exato do que o modelo original, ainda há espaço para melhorias. Isto pode ser conseguido através da avaliação de imagens de satélite com uma pluma limpa e os ficheiros de registo dos navios devem estar disponíveis. Poderá tentar-se calcular um termo de fonte de pico de transbordo ajustável utilizando o ciclo de feedback para melhorar a precisão do modelo e a gestão ambiental em projectos de dragagem. Em conclusão, as imagens de satélite são uma ferramenta valiosa para a melhoria de modelos de transporte sedimentar.

Palavras-chave: imagens de satélite, turbidez, modelos de plumas de dispersão de sedimentos, dragagem, termo fonte.

SUMMARY

The dredging industry is essential for land reclamation, coastal protection, navigation, and environmental remediation. However, dredging activities generate suspended sediment plumes that can have economic, social, and environmental impacts. Various types of dredgers, including trailing suction hopper dredgers (TSHDs), generate these plumes, which consist of fine particles suspended in the water column. These plumes affect local ecosystems by reducing light availability and oxygen levels and damaging, for example, seagrass, and corals. As a precaution, Environmental Impact Assessments (EIAs) are carried out to analyse potential impacts and ensure compliance with regulations.

Far-field sediment transport models are used to estimate total suspended solids (TSS) as a proxy for turbidity. These models, however, are subject to uncertainty due to unknown sediments conditions and the complexity of plume development processes. One factor of uncertainty is the source term, which represents the sediment flux released during dredging operations. Accurate estimation of this term is challenging due to the complex nature of sediment dynamics and the variability of dredging activities. The Becker method, which involves empirical calculations, is commonly used but introduces uncertainties because it does not take the specific local circumstances into consideration.

Sediment transport in dredging plumes is classified into dynamic near-field and passive far-field phases. Density and vessel interactions influence the dynamic near-field, while ambient hydrodynamics govern the passive far-field. Accurate modelling requires separate approaches for near- and far-field processes. Far-field models such as Delft3D and MIKE use large-scale simulations to predict sediment dispersion, but they face challenges in estimating source terms, dispersion factors, and fall velocities.

Satellite imagery could enhance sediment plume modelling by providing real-time data on plume extents. The conversion of satellite bands to surface turbidity TSS concentration values could aid in the calibration of sediment transport models. Thus the conversion of satellite bands opens the possibilities for feedback loops. Comparing model accuracy during both planning and executable phase. By incorporating satellite data, Boskalis aims to strengthen its toolkit for managing dredge plumes.

This research aims to improve sediment dispersion parameter selection for Delft3D far-field models by using techniques from AbuShanab (2022) and Boersma (2023). A proof of concept was developed for an existing project in the Philippines. Key objectives included:

- Defining the source term, dispersion factor, and fall velocity assumptions.
- Enhancing parameter definitions based on satellite imagery analysis.
- Evaluating model accuracy and improvement.
- Creating a feedback loop for continuous model refinement.

This study demonstrated that satellite imagery can help improve the accuracy of sediment transport models. The model that would be simulated in the planning and design phase (PD model) showed high uncertainties in TSS concentrations and in the plume extent % compared to the satellite-based model (SB-model). The satellite imagery is utilised for analysis of the plume behaviour, determining the background concentration values, maximum concentration values and distinguishing the vessels displayed in the imagery with additional help of AIS vessel tracks. With this information and the use of log files, when available, the additional information from the satellite images is utilised to calibrate the SB model. Creating profile plots along the AIS vessel tracks, difference plots and analysis parameters like RMSE, R^2, bias and plume extent % calculations. The SB-model differed from the PD-model in the peak overflow source term 80% exceedance value (P80), plume positioning, IM fraction distribution and dispersion factor. The P80 value was lower than the predicted value and was set to release along the AIS vessel track every minute relative to the stationary source term of the PD-model. The IM fractions of the SB-model were IM1 33% IM2 66% whereas the PD-model had IM1 66% and IM2 33% and the dispersion factor was set to 3 m^2/s instead of 1 m^2/s.

Although the SB-model is already more accurate than the original model, there is still room for improvement. This can be achieved by evaluating satellite images with a clean plume and the ship log files should be available. An attempt could be made to calculate an adjustable Peak Overflow source term using the feedback loop to improve model accuracy and environmental management in dredging projects. In conclusion, satellite imagery is a valuable tool for refinement of sediment transport models.

Keywords: Satellite imagery, turbidity, sediment dispersion plume models, dredging, source term.

TABLE OF CONTENTS

LIST OF FIGURES AND TABLES

LIST OF EQUATIONS

ABBREVIATIONS

ADCP	Acoustic Doppler Current Profiler
AIS	Automatic Identification System
ASCII	American Standard Code for Information Interchange
EIA	Environmental Impact Assessment
Delft3D FM	Delft3D Flexible Mesh
DelWAQ	Delft3D Water Quality
FNU	Formazin Nephelometric Unit
IHO	International Hydrographic Organisation
ISA	International Standard Atmosphere
MMSI	Maritime Mobile Service Identity
MODIS	Moderate Resolution Imaging Spectroradiometer
NTU	Nephelometric Turbidity Unit
PD	Planning and Design phase
QGIS	Quantum Geographic Information System
R^2	Square Root (Coefficient of determination)
RMSE	Root Mean Square Error
SB	Satellite Based
SDG	Sustainable Development Goals
SNS	San Nicolas Shoal
SPM	Suspended Particulate Matter
TSHD	Trail Suction Hopper Dredger
TSS	Total Suspended Solids

1| INTRODUCTION

1.1 Background

The dredging industry is a global industry that focuses on the removal and deposition of sediments. It is employed for land reclamation, the protection of coasts, navigational purposes, and the recovery of environmentally impacted areas by the removal of silt, toxins, and pollutants from the water bottom (Raunek, 2023).

Dredging is conducted by a variety of dredging vessels, including Trailing Suction Hopper Dredgers (TSHD). They can produce suspended sediment plumes due to the discharge of fine particles at the suction head (Boersma, 2023). Suspended sediment is carried by the water column, with turbulent eddies preventing particle settling. Additionally, these plumes can be generated through overflow from the hopper, transportation, and dumping (Becker, 2015). Therefore, the practice of dredging can have a multitude of consequences on economic, social and environmental fronts.

1.2 The impact of dredging

According to the International Association of Dredging Companies, the latest Dredging in Figures total turnover for 2022 was estimated at €6.09 billion. This represents a 14% increase in comparison with the previous year. It is anticipated that the number will increase due to population growth and demographic changes, which will result in an increased demand for products and services. Moreover, the necessity for coastal protection will increase as a consequence of the intensification of adverse weather patterns and the rise in sea levels. Finally, the development of infrastructure is essential for the exploitation of offshore energy resources such as wind energy (IADC, 2023).

The focus on dredging impacts on local ecosystems and environmental aspects for sustainable development was first introduced in the 1980s and further reinforced by the United Nations' Sustainable Development Goals (SDGs) in 2015. It actively integrates socioeconomic and environmental considerations into projects to address environmental impacts and meet legislative and stakeholder expectations (United Nations, 2015; Willemsen, 2022). Dredging

activities contribute to environmental impact in various ways. Firstly, increased sound levels can affect the behaviour of fish, with subsequent adverse effects on aquatic life. Secondly, emissions, including greenhouse gases and pollutants, and the release of contaminants have been observed to have a negative impact on aquatic life (Wenger *et al.*, 2017).

In the context of environmental dynamics, dredging plumes can result in the reduction of available light and a decrease in oxygen levels in the surrounding waters. This can lead to the harm of local ecosystems, including seagrass, phytoplankton, fish and corals, when sediment particles fail to settle (Erftemeijer *et al.*, 2012; Smith *et al.*, 2019). To quantify these impacts, an Environmental Impact Assessment (EIA) is often conducted, with the aim of providing a detailed analysis of the potential environmental consequences of a project. EIAs are therefore particularly relevant for regulatory approval and monitoring design (Boersma, 2023). The identification of sensitive receivers, the determination of their turbidity thresholds, and the reliable prediction of increased turbidity from dredge plumes are crucial elements in the process of assessing the environmental impact of dredging activities (Sun et al., 2020).

1.3 Problem description

To assess the limits of the sediment plume, far-field sediment transport models are constructed and the process governing the plume behaviour in the passive phase is monitored. The models are used to make Total Suspended Solid (TSS) estimates as a proxy for turbidity. The TSS predictions have large uncertainties due to the lack of knowledge of the exact soil conditions and the amount of fines released that will be encountered during dredging. The turbulent overflow situation is also difficult to model due to the complex mix of processes governing plume development(Willemsen, 2022) and combining near and far-field models.

1.3.1 Sediment Transport

By examining a dredging plume, it is possible to distinguish between the dynamic near-field and the passive far-field. This distinction has been made by various researchers, including (Laboyrie et al., 2018 and Sun, et al. , 2020). The dynamic near-field is density-driven and entrained by ambient water, and it interacts with the vessel. The passive far-field is influenced by ambient hydrodynamics and settling dynamics. In practice, the distinction between a dynamic and passive plume is not clear-cut. A plume may exhibit a gradual reduction in its

dynamic character until it is solely governed by ambient hydrodynamics. This transition marks a shift from a dynamic to a passive plume classification. However, the distinction between these two types of plumes is important from a modelling standpoint. Due to the significant differences between near- and far-field processes, these processes are typically modelled using separate modelling approaches. This research will focus on far-field modelling, which employs large-scale models such as Delft3D and MIKE. Far-field modelling presents certain challenges, including the accurate estimation of the source term, dispersion factor and fall velocity (Willemsen, 2022).

The source term represents the quantity of sediment fluxes released into the water during dredging. In the case of the far-field, this term is based on the suspended sediment entering the far-field as discussed by Becker et al. (2015) and de Wit (2015). To calculate the far-field source term, the empirical method proposed by Becker is frequently employed. The Becker method comprises several steps, each of which introduces a degree of uncertainty. The potential source is initially identified by determining the type of dredging equipment (e.g., TSHD) and the employed process. The second step is to calculate the total mass of fines present within the dredge volume, utilising in-situ measurements and soil properties.

In short, the source term is dependent upon the production of the vessel, the dry bulk density of sediment, the quantity of fines present (in percentage terms) and the source term fractions. The source term fraction represents an empirical coefficient with a value between 0 and 1, which describes the proportionate amount of fines that will ultimately be dispersed within the water column. The distribution of available fines among the work method elements varies according to the specific type of equipment in question (Table 1). The initial reference point for each equipment category is the total mass of fines (dry solids) present in the soil.

Table 1: Ranges for the empirical source term fractions, according to Becker (2015).

Plume source	**Symbol**	**Fraction**
Draghead	σ_d	0-0.03
Overflow ratio	R_o	0-1
In-hopper-settlement	F_{sett}	0-1
In-matrix fixation	F_{trap}	0.01-0.05
Overflow	σ_o	0-0.02
Cutterhead	σ_c	0.01-0.05
Bucket drip	σ_b	0-0.04
Bottom door (hydraulic)	σ_p	0-0.1
Bottom door (mechanical)	σ_p	0.0-0.05

In the final stage of this process, the source term estimates are applied to the computational grid of the far-field model to evaluate its dispersion. In order to ensure the accuracy of the results, it is essential to consider the numerical(times step, grid discretization) and physical aspects(depth release, capture of hydrodynamics) of the model (Becker et al., 2015).

In addition to the aforementioned uncertainties, the fall velocity and dispersion factor also contribute to the overall uncertainty of the model. The rate at which sediment particles settle is known as the fall velocity, which influences sediment transport and deposition patterns. The dispersion factor (typically 1 m^2/s for 3D calculations) plays a role in determining the characteristics of a sediment plume. This factor represents an estimate of the turbulent diffusion of sediment particles within the water column. Adjustments to this factor influence the spatial distribution and spreading of sediment concentrations, potentially leading to low-concentration, diffuse plumes, or high-concentration plumes with sharp edges.

1.3.2 Satellite imagery

The use of satellite imagery could make it easier to implement source terms, fall velocity, and dispersion factors in far-field models. This could be achieved by examining the sediment plumes in a project's performance and monitoring stage, thereby creating a feedback loop to enhance the planning and design (see Figure 1). WaterInsight developed an algorithm that is capable of determining the TSS of a Sentinel-2 satellite image. By examining satellite images during dredging operations, the displayed plumes could assist in improving the estimates and uncertainties in sediment plume models (Peters et al., 2021).

In-situ measurements provide highly accurate data and can offer real-time information, but they are expensive and logistically challenging. Satellite images cover large areas and are cost-effective but may lack detail and can be affected by weather conditions. The Becker method may not capture all complexities and requires calibration with actual data, which may not always be available (Becker et al., 2015).

Combining in-situ measurements, satellite imagery, and models can leverage the strengths of each method. Satellite imagery provides broad coverage and frequent updates, in-situ measurements offer high accuracy, and models help in understanding processes and making predictions.

1.3.3 Feedback loop

A high-frequency feedback loop (Figure 1) can assess the model's accuracy by comparing it to satellite images produced during the planning and design stages. Both the “Execution”, and “Planning and design” phases can employ the newly calibrated model and improved values.

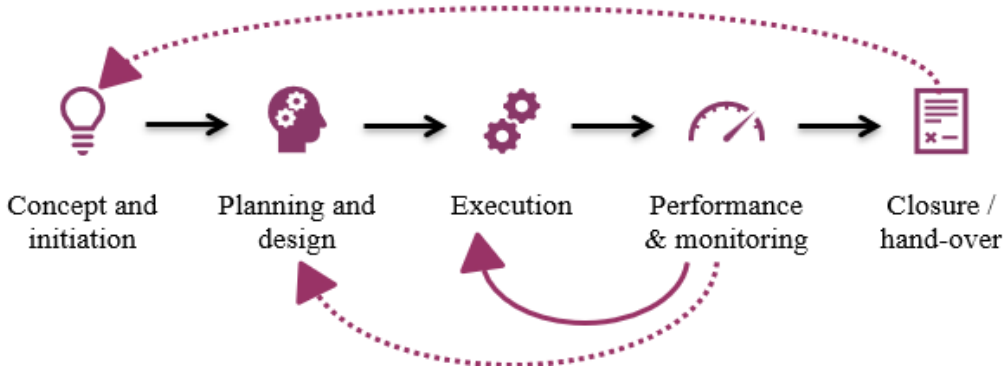

Figure 1: Project life cycle with a high frequency feedback loop to improve execution - operational modelling.

At the moment, Boskalis[1] uses various predictive techniques, monitoring programmes, and adaptive management measures to proactively control the environmental effect of dredge plumes on projects. Using satellite images, the toolkit for regulating dredge plumes is intended to be strengthened. This dissertation investigates the use of satellite imagery to enhance dredge plumes' comprehension and forecasting abilities.

[1] Boskalis is a leading international provider of maritime services and dredging contractors. While upholding the highest safety and sustainability standards, offering creative and competitive solutions to the offshore energy industry, ports, and coastal and delta regions of the world (Boskalis, 2024).

1.4 Research Objectives

The goal of this research project is to improve the selection of sediment dispersion parameters for Delft3D modelling of dredge plumes through the application of techniques outlined by AbuShanab (2022) and Boersma (2023). To achieve that goal, the techniques to be used include in-situ data analyses for better understanding the hydrodynamic processes affecting the sediment dredging plumes, application of numerical modelling, the Becker method, comparing a sediment dispersion model with satellite image TSS values and existing models, and creating a feedback loop.

Considering this, the primary research question that is addressed is as follows:

To what extent can model assumptions related to sediment dispersion parameters be improved using plume extents derived from satellite imagery?

The question is investigated in relation to an existing project. To answer the main question, a series of sub-questions are posed and answered with reference to the case study.

What parameters were assumed to develop a source term for the Delft3D model of the sediment plume? Specifically, what range of values were used for the source term, dispersion factor, and fall velocity?

How could the aforementioned parameters and their values have been better defined based on the analysis of plumes from satellite imagery?

What was the degree of accuracy of the Prediction and design phase model (PD-model), and by how much was it improved?

What would be the best way to create a feedback loop using satellite imagery to improve the accuracy of the plume prediction models?

1.5 Thesis structure

This thesis incorporates a number of technical components, as well as the development of modelling tools and approaches. It follows a traditional thesis structure, comprising a theoretical framework, a description of the study area, the methodology, the results, a discussion, and the conclusions (see Figure 2).

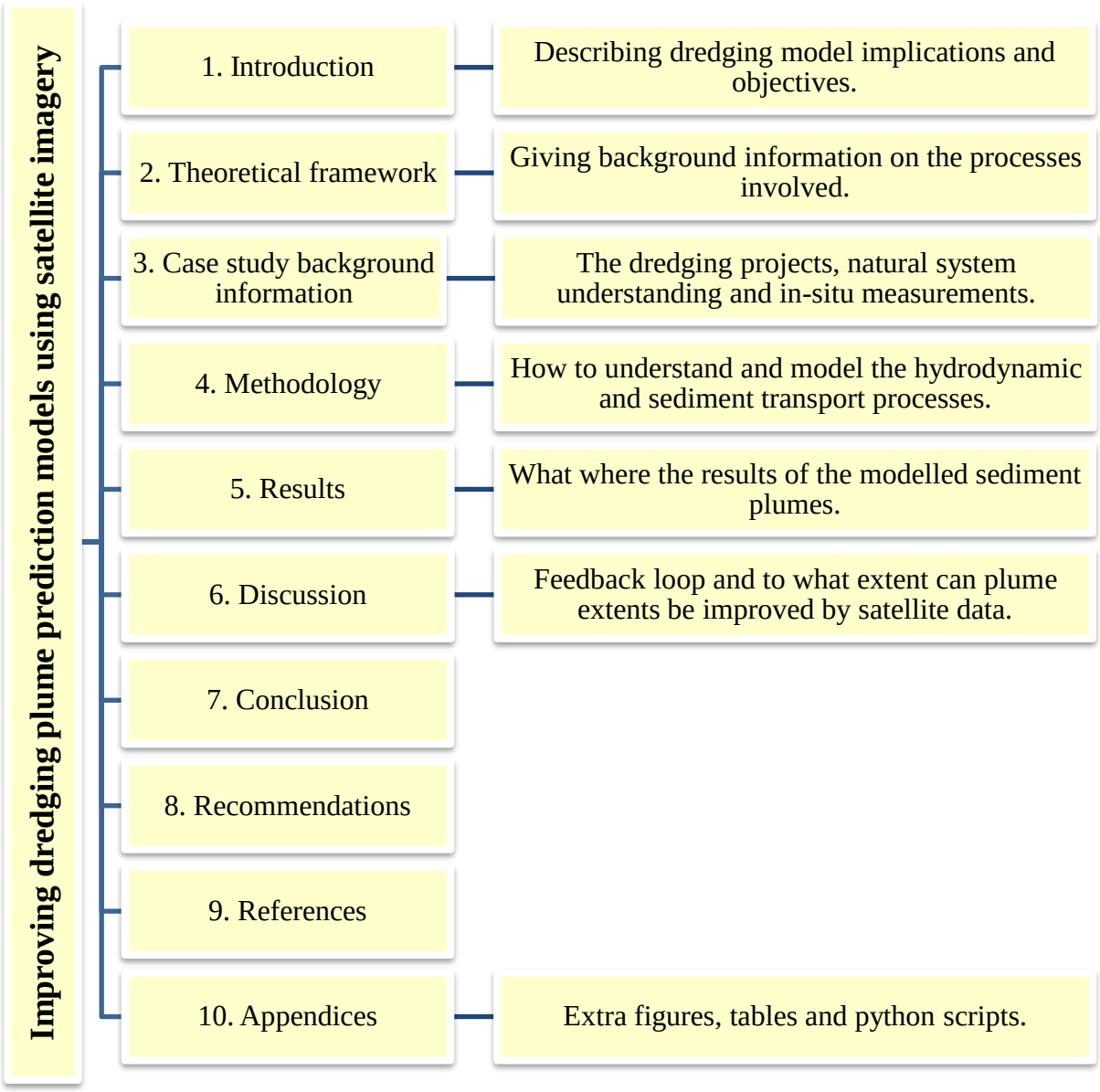

Figure 2: Structure of the thesis.

2| THEORETICAL FRAMEWORK

2.1 Introduction

A review of the existing literature on the use of satellite imagery to derive sediment plumes reveals a limited number of studies in this domain. Although a few papers have addressed this topic, the application of satellite imagery to improve model predictions and accuracy remains underexplored. This chapter presents an overview of existing research on this topic and highlights areas where further investigation is required.

2.2 Process description

Central to improved sediment plume prediction is a sound understanding of the dredging process. The characteristics of different types of dredgers vary significantly. For instance, their operational sensitivity to factors such as waves and currents, their minimum water depth requirements, their horizontal channel dimensions, their ability to function in specific soil types, the rates at which they are capable of producing a dredged bed profile, and their accuracy in achieving this profile are all important factors (van Rijn, 2023).

Dredgers can be classified into four categories: hydraulic, mechanical, mechanical/hydraulic, and hydrodynamic (Willemsen, 2022).

- Hydraulic Dredgers utilize centrifugal pumps to excavate material from the seabed. The suction dredger is the simplest of these types.
- Mechanical Dredgers: Employ mechanical excavation equipment and include:
    - Grab Dredger: Features a cable crane mounted on a vessel.
    - Bucket Ladder Dredger: Uses a rotating chain of buckets to excavate and lift material.
    - Backhoe Dredger: A hydraulic excavator mounted on a pontoon.
- Mechanical/Hydraulic Dredgers: Additionally centrifugal pumps are employed and can be classified in two categories:
    - Cutter Suction Dredger: Equipped with a rotating cutter to remove harder soils from the bottom.

    - The Trailing Suction Hopper Dredger (TSHD) uses the ship itself to transport the dredged material to the relocation site, where the load is then deposited. TSHDs are commonly used for capital and maintenance dredging.
- Hydrodynamic Dredgers: These are less suitable for use in sensitive areas. An example is the Water Injection Dredger, which injects water into the seabed to resuspend sediment and facilitate its transportation and subsequent settlement downstream.

This research will focus on the TSHD (hydraulic dredger) . The TSHD makes use of hydraulic methods, which involve a self-sailing vessel equipped with suction pipes and a drag head suspended from cables. This allows the machine to be effective in the excavation of relatively soft, unconsolidated soil, making it a suitable option for use in large-scale channel maintenance projects. The TSHD can be equipped with unloading options such as pipeline pumping and rainbowing, as detailed by van Rijn, (2023).

As discussed in the previous sections the dredging activities of the TSHD result in increased concentrations of suspended sediment. This leads to a number of environmental challenges. Of these challenges, hopper dredging is identified as one of the most turbidity-generating methods (van Rijn, 2023), particularly due to overflow, and this results in the formation of suspended sediment plumes. As the hopper fills with the dredged mixture of water and sediment, the water level rises and starts to overflow back into the ocean. By removing excess water, the dredger can carry more sediment per trip, making the operation more efficient. However, the overflow typically contains a high concentration of very fine particles that form a turbidity plume.

Plumes can be either passive (dispersing to the far-field as a density current) or dynamic (settling quickly and impinging on the bottom in the near-field). Typically, only a small proportion (3-5%) of the very fine material remain in suspension and reach the far-field given their low settling velocities. However, passive plumes are of principal concern from an environmental perspective given that their spatial and temporal scales are larger than those of dynamic plumes. Passive plumes are formed by the mixing of the dredge plume with ambient water, facilitated by robust current velocities that disseminate particles throughout the water column. They exhibit behaviour akin to buoyant gas plumes and waste plumes in open water systems, with the dynamic plume transitioning to a passive state in the near-field of the dredging operation (Becker et al., 2015).

Blaas et al. (2007), Son et al. (2014) and Mendoza et al. (2018) emphasise the impact of wind, waves, and local hydrodynamic conditions on the behaviour of sediment plumes in marine environments. The behaviour of these sediment plumes in marine environments is influenced by a number of factors, including wind and wave patterns. The availability of sediment for horizontal transport is subject to control by local atmospheric weather conditions, including wind and solar radiation. The occurrence of strong winds can result in increased turbulence and mixing, which in turn affects the horizontal transport of suspended sediments. Furthermore, the behaviour of sediment plumes can be influenced by waves and shear. When vertical mixing is strong due to wave action, suspended sediments are diluted, and the amount available for horizontal transport is reduced. These factors, in conjunction with local oceanic hydrodynamic conditions, such as tides, can impact the dispersion and transport of sediment plumes in marine environments (Kim *et al.*, 2018).

2.3 Modelling approaches

Models are employed to assess the environmental impact of dredge plumes to ensure that they dissipate sufficiently before reaching sensitive receivers like seagrass. Models can be distinguished according to their application in the far-field or near-field, as well as their focus on hydrodynamic or sediment transport processes. A hydrodynamic model is capable of reproducing a number of key variables, including waves, flow velocity and bed shear stresses. The sediment transport model is linked to the hydrodynamic model in a manner that is both a direct and indirect influence on the sediment plume. When the requisite model input and parameters (source term, fall velocity, dispersion factor, etcetera) are provided, the sediment transport models are capable of solving the dynamics of plume sediment (Becker *et al.*, 2015).

Far-field hydrodynamic models are employed to monitor the behaviour of sediment plumes in the far-field. As illustrated in Figure 3, these models are adopted from the transition of the dynamic to the passive phase. They resolve continuity and momentum equations in time for the fluid as well as for the sediment on a specified grid. These models are appropriate for the dispersion and behaviour of suspended sediment at a distance from the dredging source. Conversely, far-field models are unable to fully resolve near-field effects, such as the dynamic processes associated with the immediate release of sediments from the dredging equipment. Specific interactions, such as density currents, propeller wash effects, and other immediate complexities, are more effectively addressed through near-field modelling (Becker et al., 2015).

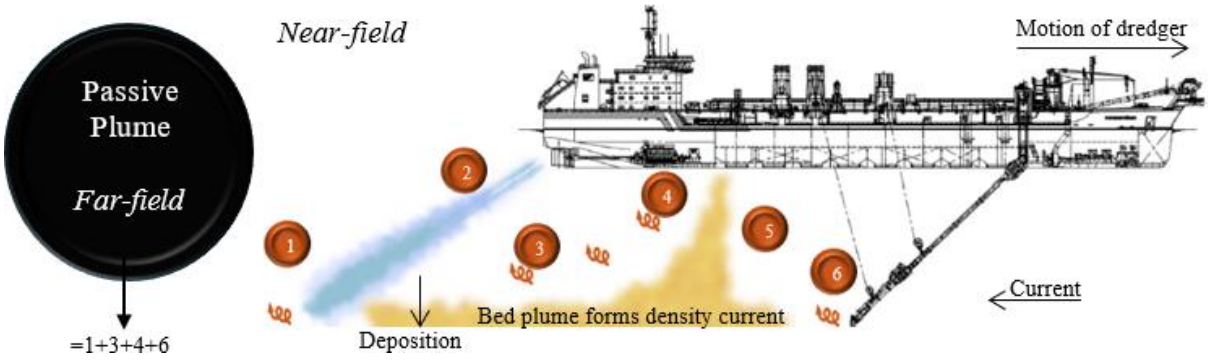

Figure 3: Scheme showing the transition from dynamic to passive phase, which defines the far- and near-field of a Trailing Suction Hopper Dredger (adapted from Becker et al., 2015). 1) Erosion of bed by propellor jet, 2) Mixing of plume by propellor jet, 3) Re-entrainment of bed plume, 4) Surface plume, 5) Dynamic plume, 6) Drag head plume. The passive plume exists out of 1, 3, 4 and 6.

A large-scale area model such as Delft3D is effective at simulating passive far-field processes on a large spatial and temporal scale (de Wit et al., 2020). The utilisation of 2D or 3D nonlinear shallow water equations allows for the assumption of hydrostatic pressure and the solving of advection-diffusion equations for passive sediment transport. While these models are well-developed, it is essential to exercise caution when considering domain dimensions, grid sizes, and diffusion coefficients in order to achieve accurate far-field modelling (Tuinhof, 2014). Despite recommendations for fine-grid 3D models, which require computing power and time, more cost-effective alternatives to near-field modelling, such as empirically calculated source terms may be viable (Willemsen, 2022). Large-scale models may lack the requisite resolution for the precise representation of dynamic phase processes in the near-field, thereby necessitating input to the far-field model in the form of a source term (in kg/s) for suspended sediment of dredging plumes (Becker *et al.*, 2015).

Accurately estimating the source term, defined as the quantity of sediment entering the far-field during dredging operations, is of paramount importance for conducting comprehensive environmental assessments. However, this task is inherently challenging due to the variations in dredging conditions and the lack of consistency in estimation approaches (Sun et al., 2020). Furthermore, the accurate implementation of source terms in far-field models, particularly the determination of the appropriate input location and the resolution of challenges in spatial transitions, represents a significant obstacle. This necessitates informed decisions on dimensions, grid sizes, and distribution to enhance prediction accuracy (Tuinhof, 2014; Willemsen, 2022).

One practical method to address these challenges is the source term fraction concept, as proposed by Becker (2015). This approach offers a generic method for estimating far-field source terms, particularly since detailed near-field modelling is computationally expensive. As described in Section 1.3.1, this method entails empirically tracking the fate of fines in dredged material across various operational stages, employing source term fractions to correlate contributions to the overall far-field source term. Consequently, addressing these challenges is critical for improving the reliability of sediment dispersion models and ensuring effective environmental management during dredging operations.

2.4 Traditional monitoring methods

While far-field modelling is typically adopted to predict dredge plumes and facilitate decision-making in planning dredging activities, often the actual dredge plumes are monitored during the dredging work to assess the dredging impact. Plumes are typically monitored with in-situ turbidity measurements or TSS samples. Despite monitoring efforts, in-situ measurements are rarely used in practice to validate predictive far-field modelling. This is because the measurement equipment is only installed just before dredging operations start and the sediment transport models are produced in the planning and design phase.

The suspension of sediments in a liquid causes an increase in particle concentration and a decrease in transparency (or conversely an increase in turbidity). These changes in water clarity can be quantified using a range of techniques, including visual observation, optical backscatter, and physical measurement.

One of the earliest techniques employed to assess turbidity was the Secchi disk, a visual method that remains in use today. This entails lowering a white or white-and-black painted disk into the water until it is no longer visible. The depth at which this occurs is documented, and the turbidity can be calculated. Presently, turbidity is often measured with a nephelometer, for which the standard unit of measurement is the Nephelometric Turbidity Unit (NTU) or the Formazin Nephelometric Unit (FNU). A lower NTU or FNU value corresponds to clearer and less turbid water.

While turbidity takes into account water's optical properties, it is not a direct measure of suspended sediments. Turbidity is an indirect measure of the presence of particles, whereas TSS measurements directly quantify the mass of particulates in water. The most common method for measuring TSS is the gravimetric method, which involves taking water samples, filtering, drying, and weighing the remaining solid particles. TSS values (mg/l) are typically in the order of 2-5 times turbidity values (NTU). These correlations are highly site-specific and are important for relating turbidity measurements to modelled TSS predictions.

In-situ measurements continue to be a critical tool in the study of sediment dynamics, even if techniques have evolved and become more sophisticated. For example, Spearman et al. (2020) utilized an array of instruments to investigate the initiation and tracking of sediment plumes. Their set-up included:

- A bespoke benthic lander equipped with four optical backscatter sensors (OBS),
- An upward-looking Acoustic Doppler Current Profiler (ADCP),
- A remotely operated underwater vehicle (ROV), and
- An autonomous underwater vehicle (AUV).

This combination of equipment was used to collect data and monitor sediment dynamics in the underwater environment. While the integration of these systems enables effective tracking of sediment plumes, it is important to note that this approach involves significant costs. Moreover, these measurements are typically limited to specific points unless a large number of systems are deployed.

For large-scale analyses, a high number of such systems would be required. Additionally, samples of water and Total Suspended Solids (TSS) must be collected to validate the OBS data.

According to practical experience, this validation process is complex and varies significantly depending on the type of sediment. Thus, while these sophisticated systems can provide detailed insights into sediment dynamics, their deployment on a large scale poses logistical and financial challenges. The process of collecting and validating TSS data further adds to the complexity, emphasizing the need for meticulous planning and execution in such studies.

2.5 Turbidity and TSS concentrations from Remote sensing

Remote sensing technologies are increasingly recognized for their ability to assess and monitor environmental impacts in estuarine and coastal waters (Caballero et al., 2018). The integration of satellite imagery, especially through a multi-sensor approach employing both medium- and high-resolution satellites alongside atmospheric correction processing, has shown considerable promise in various applications. These include monitoring dredging activities, assessing turbidity, and estimating sediment concentration in coastal and inland waters. Herein, we discuss the various aspects and advancements in this field, drawing on recent research and case studies.

Satellite imagery can significantly enhance traditional monitoring methods by providing more accurate source terms, dispersion factors, and settling velocities for dredge plumes (Boersma, 2023). While traditional methods have their merits, the ability of satellite imagery to cover large spatial areas and provide frequent observations makes it a valuable tool in environmental monitoring. Compared to traditional physical monitoring methods, remote sensing techniques are also noninvasive and minimally disturb or alter sediment concentrations during measurement.

Recent studies have employed both drone and satellite imagery to measure dredge-induced turbidity, albeit with some limitations. Hayes et al., (2022) recommend combining drone data with in-situ measurements to achieve greater accuracy. The use of the single red band approach (Dogliotti *et al.*, 2015) in drone data processing has shown promise, especially in reducing benthic interference. However, the depth range and accuracy remain limited when relying solely on drone data.

Identifying sediment plumes using satellite data involves isolating the dredging plume from other optical elements like wind, tidal forces, and riverine outflow. Institutions have utilized Landsat and MODIS data for this purpose, but challenges persist due to inadequate historical baseline data and environmental factors such as clouds and sensor zenith angles. Specific wavelengths, such as 667 nm for MODIS and 655 nm for Landsat, may also influence the accuracy of results, with recommendations to use 865 nm data in certain scenarios (Barnes et al., 2015).

Several satellite systems can be employed to monitor TSS anomalies in coastal and inland waters. These include Landsat-8, Sentinel-2A, WorldView-2, WorldView-3, and GeoEye-1 (Caballero et al., 2018). Where cost is a constraint, systems are typically characterized by differing trade-offs between spatial and temporal resolution i.e. where higher spatial resolution often results in lower temporal resolution and vice versa. The following table (Table 2) summarizes the key characteristics of different satellite systems.

Table 2: Differences between Landsat-8, Sentinel-2A, WorldView-2, WorldView-3, and GeoEye-1, focusing on resolution, frequency of imagery, and other key characteristics.

Satellite	Spatial Resolution	Temporal Resolution	Bands	Swath Width	Strengths	Trade-offs
Landsat-8	15m (panchro.), 30m (multi.)	16 days	11	185 km	Free, long-term data	Lower resolution, longer revisit
Sentinel-2A	10m (vis & NIR), 20m (Red, SWIR), 60m (coastal)	5 days (with 2B)	13	290 km	High revisit, free	Moderate resolution
WorldView-2	0.46m (panchro.), 1.85m (multi.)	1.1 days	8	16.4 km	High resolution, frequent revisits	Costly, smaller swath
WorldView-3	0.31m (panchro.), 1.24m (multi.)	<1 day	29	13.1 km	Highest resolution, frequent revisits	High cost, smaller swath
GeoEye-1	0.41m (p), 1.65m (m)	<3 days	5 bands	15.2 km	High spatial resolution, frequent revisits	Costly, smaller swath width

A notable application of satellite imagery was conducted by Islam (2007), who used data from Landsat 7 TM, EO-1 MODIS TERRA, and AQUA to track sediment plume movements and estimate TSS concentrations during dredging operations. The study highlighted limitations in spatial resolution and signal-to-noise ratio but found the technique cost-effective and insightful for understanding sediment dynamics.

Building on this foundation, Boskalis has initiated several research projects to develop digital monitoring techniques for dredging plumes. In collaboration with WaterInsight, they are utilizing data from Sentinel-2 and Sentinel-3 satellites to create algorithms for generating near real-time total maps based on spectral data (Peters et al., 2021). Meanwhile, AbuShanab (2022), in collaboration with Boskalis, employed edge detection algorithms on satellite imagery to identify sediment plumes and compute their surface areas. This study found a positive correlation between plumes and daily spill data, though further research is needed to strengthen these findings.

Boersma (2023) advanced the field by developing a methodology to quantify source terms, sediment fall velocity, and dispersion factors using satellite imagery combined with sediment modelling. This methodology aims to enhance dredging plume prediction models.

The integration of remote sensing technologies with traditional monitoring methods holds great potential for improving the assessment and monitoring of environmental impacts in estuarine and coastal waters. Continued research and refinement of data processing methods are essential to overcome existing limitations and enhance the accuracy and reliability of these technologies.

3| CASE STUDY BACKGROUND INFORMATION

3.1 Introduction

This chapter provides an overview of the geographical context of Manila Bay. This is described to understand the natural system of the Bay and the projects located in its water before diving into the method and results. Manila Bay is positioned in the Philippines and has an average depth of 25 m and around 1800 km2 (Figure 4) (Sta. Maria *et al.*, 2009). In Manila Bay, sand was sourced for various projects from a sand borrow area. This borrow area was approximately 20 by 4.5 km, and during the execution phase, the dredging vessel would sail to the project area for sand supply.

Figure 4: Manila Bay with in the top left a key plan displaying Manila Bay's position in the Philippines and plotted in Google Earth Pro imagery.

3.2 Natural system understanding

Manila Bay is located on the southwest coast of Luzon and is a semi-enclosed body of water (Figure 4). The Bay is used for commercial, industrial and domestic activities. It has a surface area of 1800 km^2 and an average depth of 25 m. It is approximately 52 km long and 19-56 km wide (Sta. Maria *et al.*, 2009). The Bay is approximately 30 to 40 m deep in the centre and has shallow areas along the coastline.

3.2.1 Meteorological conditions

Manila Bay is influenced by the East Asian monsoon's seasonality. The monsoon causes two distinct weather seasons, namely the summer Southwest (SW) monsoon (also called Habagat from June to September) and the winter Northeast (NE) monsoon (also called Amihan from November to April). May and October are transitional months between the two seasons, as shown in Figure 5.

Habagat is characterised by winds blowing from the southwest, bringing moisture from the ocean and causing heavy rainfall during these months. Amihan has winds blowing from the northeast, resulting in a relatively dry period (Rijper, 2021).

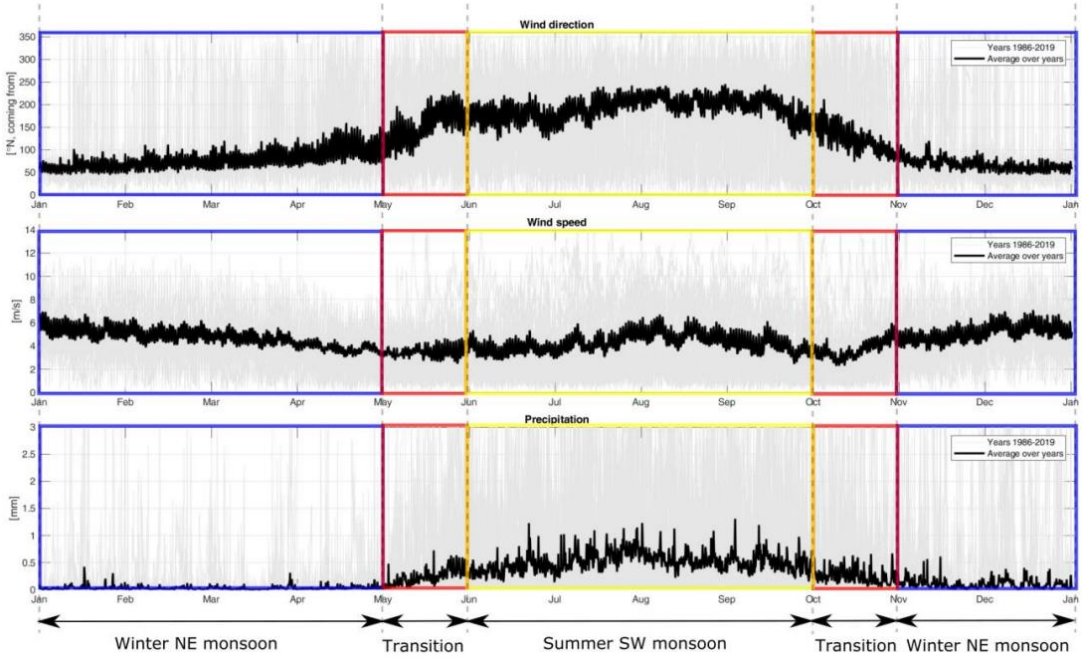

Figure 5: Hindcast data from ERA5 for wind direction (upper panel), wind speed (middle panel) and precipitation (lower panel) in the centre of Manila Bay (14.5° N, 120.7° E) (Rijper, 2021).

3.2.2 Hydrodynamic conditions

Manila Bay's hydrodynamics are influenced by tidal forces, wind-driven currents, freshwater inflows, and stratification. Tidal ranges vary from 1.6 m during spring tides to 0.8 m during neap tides. Freshwater discharge during monsoon seasons leads to significant stratification, with the northeast monsoon (October to January) and southwest monsoon (June to September) affecting circulation patterns. Surface currents during the northeast monsoon are primarily driven by wind, while deeper currents are influenced by tidal forces, leading to vertical stratification and flow reversals. A three-dimensional (3D) finite element model (RMA-10) was used to simulate circulation patterns, showing that surface currents are dominated by wind during the northeast monsoon, whereas deeper currents are driven by tidal fluxes. Radiotracer studies confirmed these findings, with tracer dispersion at 2 m of depth dominated by wind and at 15 m of depth by tidal currents (Balduzzi et al, 2016; Hughes et al., 2004. & Sta Maria et al., 2009).

Manila Bay's wave climate is characterized by moderate wave heights (0.5-1.5 m) and short to moderate wave periods (4-8 s), with significant seasonal variations (> 2 m) influenced by monsoons and occasional extreme conditions caused by typhoons. During the southwest monsoon, waves come predominantly from the west and southwest, and during the northeast monsoon, they come predominantly from the northeast. The current velocities range from 0.1 to 0.2 m/s. The complexity of Manila Bay's hydrodynamics, influenced by tidal forces, wind stress, temperature variations, and salinity distribution, necessitates comprehensive modelling and observational data for accurate assessment of the Bay (Sta. Maria *et al.*, 2009).

3.2.3 Natural turbidity levels

There is not a lot of information regarding the natural turbidity levels in Manila Bay. There has been a study regarding the NTU values near Manila Baywalk Dolomite Beach. From which is concluded that the NTU values obtained from the sampling are low to moderate with an average NTU of 11.21. It should be kept in mind that this is NTU values for shallow depths and close to the shore. When moving into the Bay the values will probably be lower (0-10 NTU) (Zulueta, 2023).

3.2.4 Sediment bed conditions

In 2009, a study of sediment accumulation rates in Manila Bay was preformed Sta. Maria *et al.*, (2009). This study conducted field sampling on 2000 and 2002 with gravity cores of 1 m and 1.5 m (7 cm approximate diameter). Collecting sediment samples across the Bay.

From the sub-samples was a grainsize analysis done taking 6 cm sub-samples for every 10 cm interval of the 1.5 m gravity core. The samples were sieved through a 63 µm mesh to separate the sand from the mud. The mud was then desalinated prior to pipette analysis. From this analysis was concluded that the sediments in the Bay are predominantly clay muddy and have a soft, fine texture. The fine sediments had a varying percentage of fines (silt) between 35 and 65 % (Figure 6) and the bulk dry density mean was 0.28 g/cm^3 with a standard deviation of 0.06 g/cm^3.

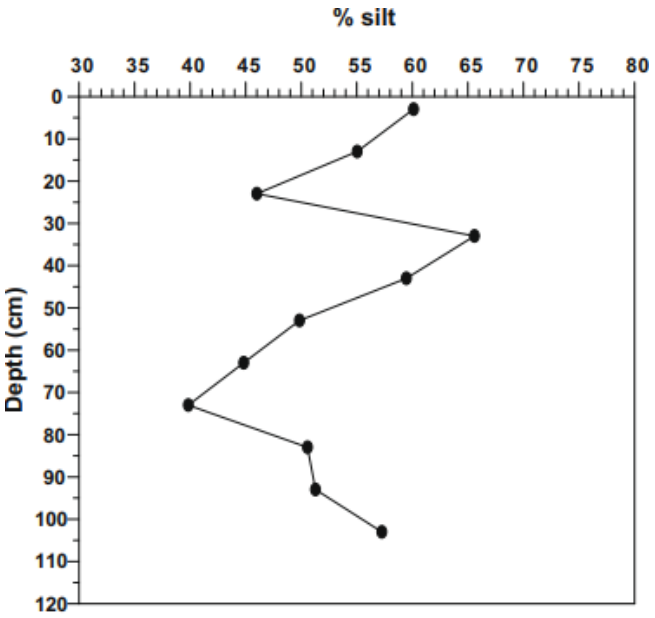

Figure 6: Silt profile of the core closest to the borrow area (silt % vs depth in cm) Source: *(Sta. Maria* et al., *2009).*

3.3 Installed equipment on-site

In Manila Bay, in-situ data was collected to verify the hydrodynamic forcing mechanisms in the borrow area. This involved the use of Acoustic Doppler Current Profiler (ADCP) equipment, as well as tidal and wind data.

The available in-situ data measurements were distributed throughout the Bay (see Figure 7). The monitoring stations include[2]:

- current data from an ADCP at monitoring station A,
- tide data from a tide gauge at monitoring station B,
- IHO data at monitoring station C (Tidal data),
- And wind data at monitoring station P1.

It should be noted that these positions are not precisely in the area of interest for the purpose of this research, which introduces additional uncertainty. The installed equipment onsite was a Nortek AWAC-1 MHz ADCP and a Valeport Model 740 tide gauge (Figure 7).

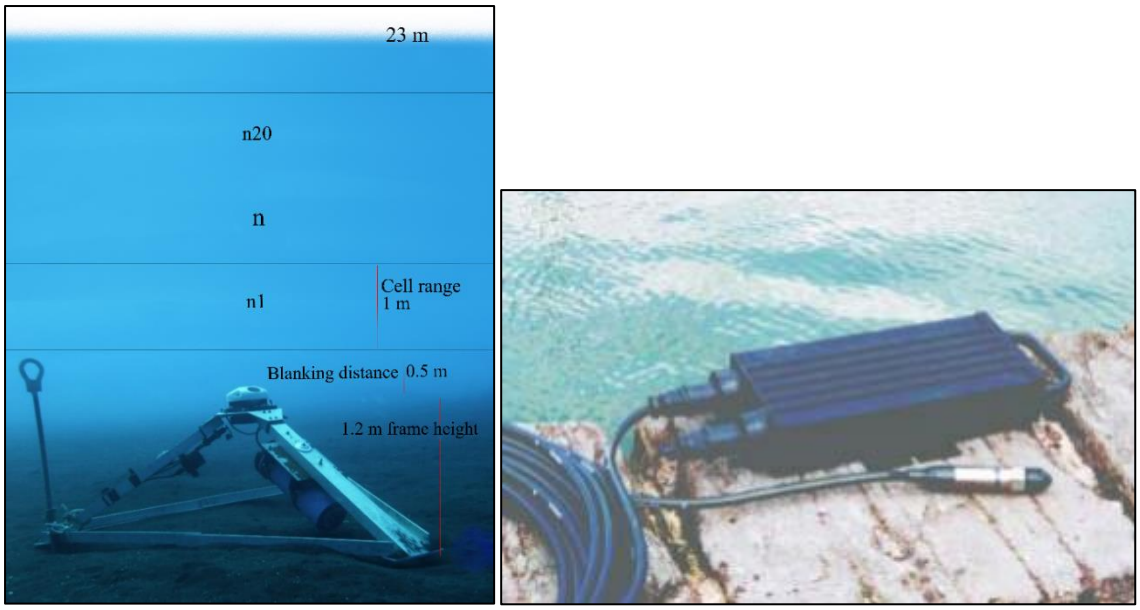

Figure 7: On the left is a representation of the Nortek AWAC-1 MHz ADCP set-up, and on the right is the Valeport Model 740 tide gauge.

[2] The equipment positions are left out due to project confidentiality.

The Nortek AWAC-1 MHz 600 kHz ADCP was mounted at monitoring station A on a 1.2 m high frame with a blanking space of 0.5 m and the cell size range set to 1 m for the water column profile. The cell size range divided the water column into discrete measurement range cells. Each range cell represented a specific depth interval. The recorded data represented the average velocity, direction within each cell to smooth out small-scale variations and provided a more stable and representative profile (for further details, see Figure 7). Data was transmitted to the datalogger at a rate of 20 minutes for time-averaged measurements. Its current speed accuracy was 0.5% and its heading accuracy was 0.2 degrees (Boskalis, 2024).

For tidal data collection at monitoring station B, Boskalis installed a Valeport Model 740 tidal datalogger, while the tidal data collection at monitoring station C was gathered from the IHO. The tidal gauge (Valeport Model 740) employed a vented strain gauge capable of measuring within a ± 0.1% accuracy range relative to its full scale. The water level data was transmitted at one-minute intervals via a UHF-synthesized radio transceiver (Boskalis, 2024). The tidal collection at position C was obtained from the IHO and presented data gathered at one-minute intervals.

The wind sensor data was obtained from the MetOcean Data Portal monitoring station P1 at a time interval of one hour (DHI, 2022).

3.4 Satellite images

Boskalis engaged the services of WaterInsight to undertake a satellite mapping exercise of Manila Bay. For mapping the area, data with a resolution of 10-60 m was available at 10-day intervals. However, the presence of clouds and sun glint occasionally interfered with the collection of data from the water surface. The occurrence of cloud cover was attributed to the monsoons, while the sun glint was the result of sunlight being reflected from the surface into the satellite sensor, which had a negative impact on the satellite imagery of water (Peters et al., 2022). Figure 8 illustrates the impact of sun glint and cloud cover on satellite imagery above water.

Figure 8: On the left is a satellite image shown without sun glint and clouds during dredging operations, while the right image shows sun glint and clouds. The right image displays turbidity along the coast, with the sun glinting at the top and clouds at the bottom.

In order to ascertain the availability of cloud-free and glint-free satellite images, WaterInsight conducted a manual examination. Based on these images, a further selection was made regarding the location and presence of dredgers, resulting in a list of 11 available satellite images for this study. The available satellite images showed dredgers from various projects.

The TSS concentration maps were produced without any local tuning of the algorithm and validated by in-situ measurements of TSS concentration data from buoys operated by Boskalis. The studies conducted by WaterInsight have demonstrated that the concentrations below 10 mg/L TSS are characterised by high levels of noise due to discrepancies between satellite and in-situ data, whereas the higher concentrations exhibited a high degree of correlation between the two datasets. The overall correlation coefficient between in-situ and satellite data was found to be $R^2 = 0.6$ (Peters et al., 2022).

4| METHODOLOGY

4.1 Introduction

In this dissertation, the approach proposed by Boersma (2023) was employed. A more detailed explanation of the methodology (Figure 9) can be found in subsequent sections. It should be noted that a model prediction of the sediment plume has already been performed for the case study, which serves as the basis for comparison with the observed plume in the satellite images.

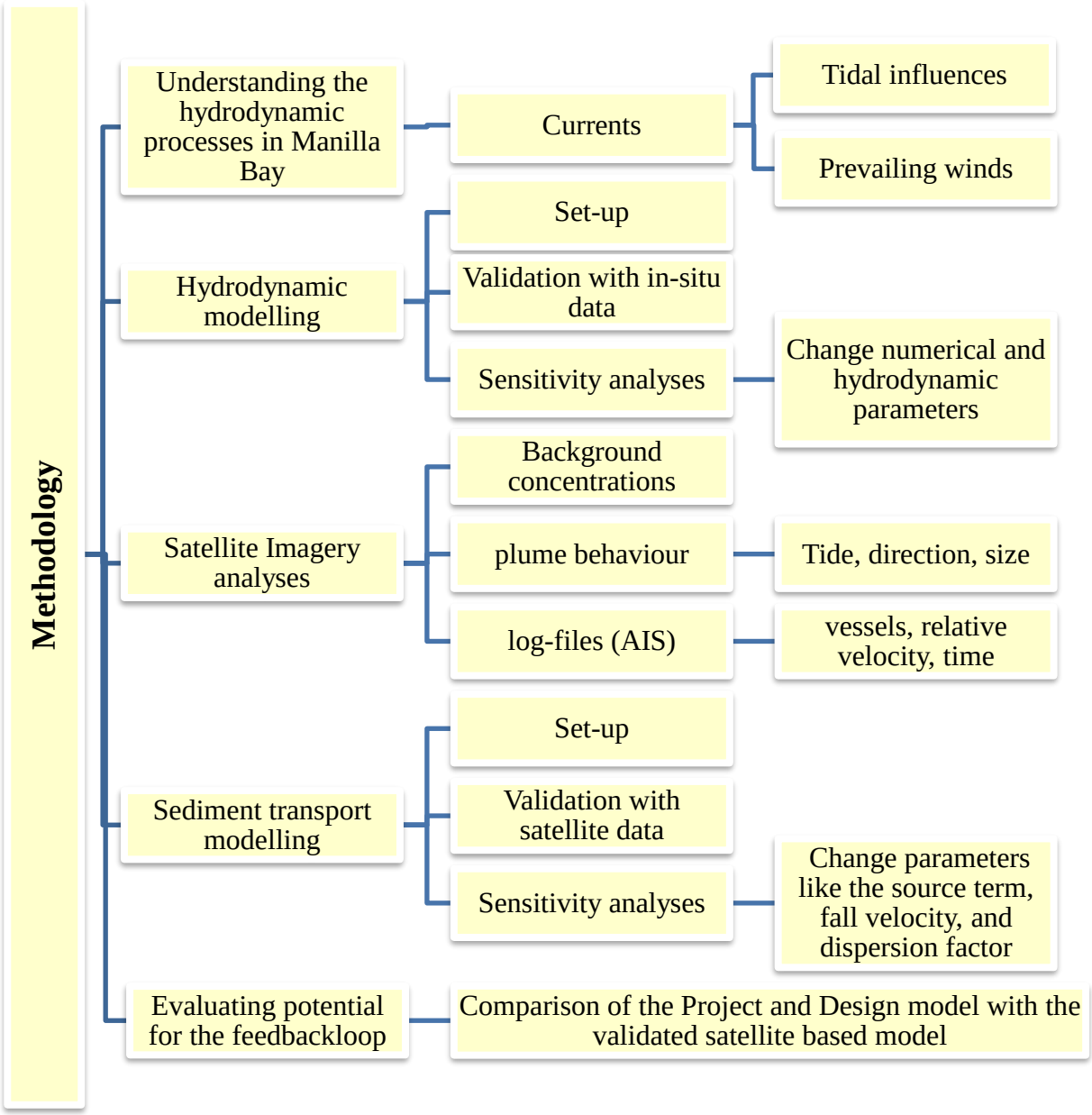

Figure 9: Method flow chart.

4.2 Used tools

Table 3 provides a comprehensive inventory of the instruments, data sources, and their respective applications used in this study.

Table 3: A comprehensive inventory of the utilized instruments and their respective applications.

	Tools, instruments
Bathymetry data	Manila Bay model made by Boskalis (Rijper, 2021)
Tidal data	Valeport 740, FES2014 & IHO
Current velocity data	Nortek AWAC-1 MHz ADCP
Wind forcing data	MetOcean data
Modelling	Delft3D FlowFM DelWAQ
Model figures & tables	Anaconda (Jupyter Notebook), Matlab, Quickplot, QGIS, Mirone.
Satellite data processing	WaterInsight, Anaconda (Jupyter Notebook), QGIS and Mirone, Panoply.
AIS-data	DevOps Boskalis World Python script

The nautical naming convention was adopted in this study to facilitate comprehension of the subsequent material (Rijper, 2021).

4.3 In-situ hydrodynamic data

Chapter 3.3 provides a detailed account of the in-situ monitoring positions and associated equipment. In order to gain insight into the hydrodynamic conditions prevailing in Manila Bay, data was collected from the various in-situ monitoring sites. The type of data available from the monitoring stations is shown in Table 4.

Table 4: Monitoring station, acquisition time interval, and type of data for each monitoring station. Note: The data was then exported into readable CSV files for further processing.

Monitoring station	Time interval	Type of data
A	1 min	Tidal water level tov MSL in m (Project data).
B	20 min	Current velocity (in m/s) and direction (in deg) (Project data).
C	1 min	Tidal water level tov MSL in m from (Public data).
P1	1 min	Windspeed (in m/s), direction (in deg), air pressure (in hPa) and rel. humidity (in %) (Public data).

4.3.1 Tidal influence

It is essential to consider tidal influence, as the tide may differ between the borrow area and the nearest tide gauge, which is approximately 40 km away. These differences will help us improve the hydrodynamic model behaviour.

The tide gauge data from the borrow area, clearly shows that the tide differs between the two locations. The relatively enclosed shape of the Bay, differences in bathymetry and river inflows are the factors that will influence tide propagation. The Bay geometry causes tidal effects to be more pronounced or attenuated at different locations. River inflows, such as the Pasig River, interact with tidal water, affecting local water levels. Monitoring stations S and C are therefore analysed to gain insights into any differences in tidal wavelength, phase, and amplitude between the two stations across the Bay. In addition, the monthly water level differences from the combined influence of spring and neap tides were also analysed. These tidal analyses provide valuable insight into the local variations of the Bay, enhancing the predictive accuracy of the water levels in the hydrodynamic model.

4.3.2 Current velocities

At monitoring station A an ADCP was deployed to analyse the current velocity and direction throughout the entire water column (25-30 m depth) in the vicinity of the borrow area. The ADCP was positioned approximately 15 km from the actual dredging area, which may result in differences in current velocity at this position. The data contains 20 layers (n1, n2, etc. chronologically from the bottom to the top layer) with current velocity and direction.

To determine the difference between the top and bottom layers of the ADCP data, the residual vectors, current speed, and direction of each layer were analysed. The current speed and direction were analysed for the period February 4th, 2023, to February 8th, 2024. Residual vectors were calculated for the top and bottom layers, showing the magnitude and direction of the current in February 2023. The residual vectors were calculated by averaging the U (zonal velocity eastward) and V (meridional velocity northward) components in February. The U- and V-vectors were calculated using Equations 1 and 2:

$$\vec{U} = magnitude * \cos(direction) \quad \text{Equation 1}$$

$$\vec{V} = magnitude * \sin(direction) \quad \text{Equation 2}$$

4.3.3 Prevailing winds

The prevailing winds differ between the summer (SW) and winter (NE) monsoons. To assess the influence of the wind on the current velocity during the period of dredging operations, MetOcean (DHI, 2022) wind data was gathered. The wind residual vector average was calculated using Equations 1 and 2, with wind speed and direction as variables. Using this data, the residual wind and current velocity were calculated for February and July 2023.

4.4 Numerical model set-up and validation

Delft3D Flow Flexible Mesh (FM) is a software that was utilized to model the hydrodynamics within the Manila Bay borrow area. The software focuses on aspects such as computational efficiency, resolution and accuracy in the simulation of water flow and related processes. To ensure that simulation results were reliable and suitable for critical decision-making in coastal and marine management, the software was designed to meet the stringent requirements of environmental and engineering guidelines (Deltares, 2024a).

Several factors can influence the hydrodynamic models, including grid size, timesteps, tide, current speed, and direction. To understand the effects of the varying parameters, the hydrodynamic model setup was optimized by performing sensitivity and validation analyses.

4.4.1 Set-up of the hydrodynamic model

Domain and Bathymetry

In order to create a computationally efficient model, the domain extents were set at 20 km outside of Manila Bay. The grid was focused on the borrow area, with a grid size of 520*520 m outside the borrow area and 65*65 m inside the borrow area. Refinement was conducted in a stepwise manner with a factor of two, with cells connected via triangular cells.

The model has been developed for the purpose of 3D plume dispersion calculations with vertical z-σ layering. The model contained a total of 10 z-σ layers, with the layer stretch coefficient being defined by the user and set to the following values: 19.5, 16.3, 13.7, 11.5, 9.6, 8.1, 6.8, 5.7, 4.8, and 4.0. Given the interest in the top layer, it accounted for 4% of the water depth, while the bottom layer accounted for 19.5%. This top layer in the model corresponded with the layer n20 from the in-situ current data. In order to create the bathymetric map, a composite of data from the GEBCO, C-Map, and client-provided surveys was used. The transition from local survey data to coarser CMAP depths was performed with the most appropriate data available. Further clarification regarding the aforementioned choices can be found in Table 5.

Table 5: Delft3D FM model input Manila Bay.

Delft3D Flexible Mesh model input		Location
Polygons	Polygon 1	Coastlines from the OpenStreetMap.
	Polygon 2	Borrow area from Rijper (2021).
Grid size	520*520 m	Outside of the borrow area.
	65*65 m	Borrow area.
Grid type	Irregular grid	Manila Bay
World (Map) system	WGS84 [EPSG:4326]	Manila Bay
Bathymetry (*.xyz file)	GEBCO	Offshore, outside of Manila Bay, resolution of approximately 450x450m.
	C-map	Manila Bay and Bay entrance, contour lines and individual points. Resolution
	Project survey data	At the project site and borrow area.
Orthogonality	Maximum 0.002	Manila Bay
Smoothness	1	Manila Bay
	3	At the borrow area connection to the refined grid.
Z-σ layers	10 layers: : 19.5, 16.3, 13.7, 11.5, 9.6, 8.1, 6.8, 5.7, 4.8, and 4.0 %.	Manila Bay

Boundary conditions

The forcing mechanisms tide and wind were added as boundary conditions to enable accurate numerical hydrodynamic model simulation of real-life conditions. The FES2014 database establishes tidal boundaries at the offshore open boundary, 20 km offshore Manila Bay, and incorporates wind MetOcean data into the model to assess the impact of wind shear and atmospheric pressure variations on water movement.

4.4.2 Validation of the hydrodynamic model against in-situ measurements

In the hydrodynamic model setup, the parameters were validated against the hydrodynamic conditions derived from in-situ measurements. Validation was achieved through the calculation of root mean square error (RMSE), adjusted R^2 (Coefficient of Determination, moving average), BIAS, correlation, plotting of predicted model conditions against observed in-situ measurements, and generating a Bland-Altman plot in Python of the top water layers (Layers 9 and 10 of the model and 19 and 20 of the in-situ ADCP measurements).

The RMSE was calculated by Equation 3, which provides an indication of the average error magnitude.

$$\mathrm{RMSE} = \sqrt{\Sigma(\mathrm{Pi} - \mathrm{Oi})^2 / \mathrm{n}} \qquad \text{Equation 3}$$

Where:

- Pi is the predicted value for the i^{th} observation in the dataset.
- Oi is the observed value for the i^{th} observation in the dataset.
- n is the sample size (Hodson, 2022).

The R^2 was calculated to determine the extent to which the variance of the actual values was captured by the predictions, as indicated by Equation 4.

$$R^2 = 1 - \frac{SSE}{SSTO} \qquad \text{Equation 4}$$

With $\mathrm{SSE} = \sum_{i=1}^{n}(y_i - \hat{y}_i)^2$ and $\mathrm{SSTO} = \sum_{i=1}^{n}(y_i - \bar{y})^2$.

- The SSE, or "error sum of squares," is a statistical measure that quantifies the extent to which the data points, y_i, deviate from the estimated regression line, $\hat{y}_i$.
- SSTO represents the "total sum of squares" and is employed to quantify the extent to which the data points, y_i, deviate from their mean, $\bar{y}$ (PennState Eberly College of Science, 2018).

The BIAS was calculated by identifying the mean difference between the actual values and the moving average predictions. This results in an average of the extent to which the predictions deviate from the actual values, indicating a systematic error. A positive BIAS indicates that the model was overestimating, whereas a negative BIAS indicates that the model was underestimating.

The correlation coefficient (R^2) determines the strength and direction of the relationship between the predicted and observed values. The coefficient is between 0 and 1 (Table 6).

Table 6: Correlation coefficient (R^2) values (Bhandari, 2023).

1	A positive correlation indicates that a change in one variable is accompanied by a corresponding change in the other variable, with the two variables exhibiting a similar direction of change.
0	There is no correlation between the variables in question.

A Blant Altman plot was employed to illustrate the correlation between two quantitative measures. This was achieved by constructing a graphical representation of the limits of agreement. The aforementioned limits were calculated by utilising the mean and standard deviations of the differences between the two measurements. This relationship was then plotted in order to ascertain whether the assumptions of normality of the differences and other characteristics were valid (Giavarina, 2015).

4.4.3 Sensitivity analyses of nonphysical and hydrodynamic parameters

The range of differing numerical model settings for several inputs can be determined by modifying the numerical model settings for the inputs in question. The impact of alterations to input variables (Table 7) on the uncertainty of the model or system output was examined by looking at the calculation time and calculating the RMSE, R^2, and BIAS in accordance with the methodology described in Section 4.3.2.

Table 7: Parameters tested for the sensitivity analysis. The values in bolt represent the values used in the calibrated scenario.

Parameter	Value
SNS grid	**65 x 65 m** 260 x 260 m 130 x 130 m
Courant number	**0.7** 0.9
Initial timestep	**1 second** 5 seconds
Z-σ layers	**10 layers** 5 layers
Wind	**ISA (**International Standard Atmosphere) **density** (1.2265 kg/m^3) **and pressure** (101330 N/m^2) Average in-situ density (1.225 kg/m^3) and pressure (101350 N/m^2)
Tide	**FES2014** TPXO7

The grid size of the model can impact the accuracy of the results, therefore, it was essential to ensure that the grid size was sufficient to demonstrate plume movement. The Courant number (Equation 5) is a dimensionless ratio that represents the ratio between a specific time interval (denoted by Δt) and the amount of time it takes a fluid particle moving at a velocity V to be conveyed throughout a cell whose dimensions are given by Δx.

$$C_0 = V\frac{\Delta t}{\Delta x}$$ Equation 5

To ensure the stability of the calculation, the Courant-Friedrichs-Lewy (CFL) criterion was taken into account. A limit of C0 <1 was imposed on the maximum value of C0 to ensure the stability of the calculation. Consequently, a higher Courant number will result in a less stable model and could lead to severe time-step limitations (Balduzzi *et al.*, 2016; Deltares, 2024b). The calibrated scenario had a Courant number of 0.7, which indicates that if 0.9 were employed, the stability of the model would decrease. The Courant number was monitored during the simulation to ensure the model remained stable.

Other numerical model parameters ascertained in the sensitivity analysis were the initial timestep and z-σ layers. To ascertain the hydrodynamic forcing mechanisms influencing the model, wind and tide parameters were introduced to check what the effect was on the current speed and direction in the model.

4.5 Satellite imagery analysis

The satellite images processed by WaterInsight were analysed using various software tools, including Mirone, Panoply, and QGIS (Luis, 2007; Schmunk Robert, 2024; 'QGIS Geographic Information System.', 2024). From the 11 available satellite images, 4 images (Figure 23) were chosen for detailed analysis based on specific criteria. The images were selected by considering the following aspects:

- Active dredging activities,
- All dredging vessels involved in dredging activities are known,
- The dredging plumes are distinguishable from one another,
- No clouds are covering the plume.

The dredging vessels involved in dredging activities in the satellite images were distinguished using QGIS. This involved loading the Automatic Identification System (AIS) data, which included the vessel trajectory (xy coordinates) and timestamps for all dredging vessels engaged in operations on the date of the satellite image. The vessels identified in the satellite images are listed in Table 8.

Table 8: Vessels dredging in each analysed satellite image. The vessels in question are TSHD 1 to 7.

Date	1	2	3	4	5	6	7
01/12/2022	X	X	X	X			
01/17/2022				X	X		X
01/22/2022	X			X		X	
03/28/2022	X						X

Upon identifying the vessels in each satellite image, the sediment plume behaviour was analysed. The analysis focused on the relationship between the sediment plume and various factors, including:

- Tide,
- Plume displacement direction,
- Residual velocity,
- Background values,
- Plume extents,
- Area of Rectangle
- Minimum concentration per plume,
- Maximum concentration per plume,

The plume displacement direction was determined by overlaying the AIS data onto the satellite image. The residual velocity of the plume was then calculated by measuring the distance between the AIS track and the plume boundaries in the direction of displacement using Equation 6.

$$v = \frac{s}{T}$$ Equation 6

The equation considers the relative velocity (v in m/s), displacement (s in m), and time (T), where time was calculated as the difference between the time of the satellite image and the time of the AIS data point (in seconds). Displacement was defined as the distance between an AIS data point and the central part of the plume (More information in Appendix B).

To further understand the plume dynamics, the size of the plume was quantitatively assessed by calculating both the area of the rectangle and the plume extents from the satellite images. The area of the rectangle was defined by the length and width of the plume in meters, while the plume extents refer to the area covered by the plume itself (Figure 10). The plume extents were calculated in m^2 as well as a percentage of the area of rectangle. Appendix E includes the code used to create the plots and calculate these parameters. (parameter values are added in Appendix F).

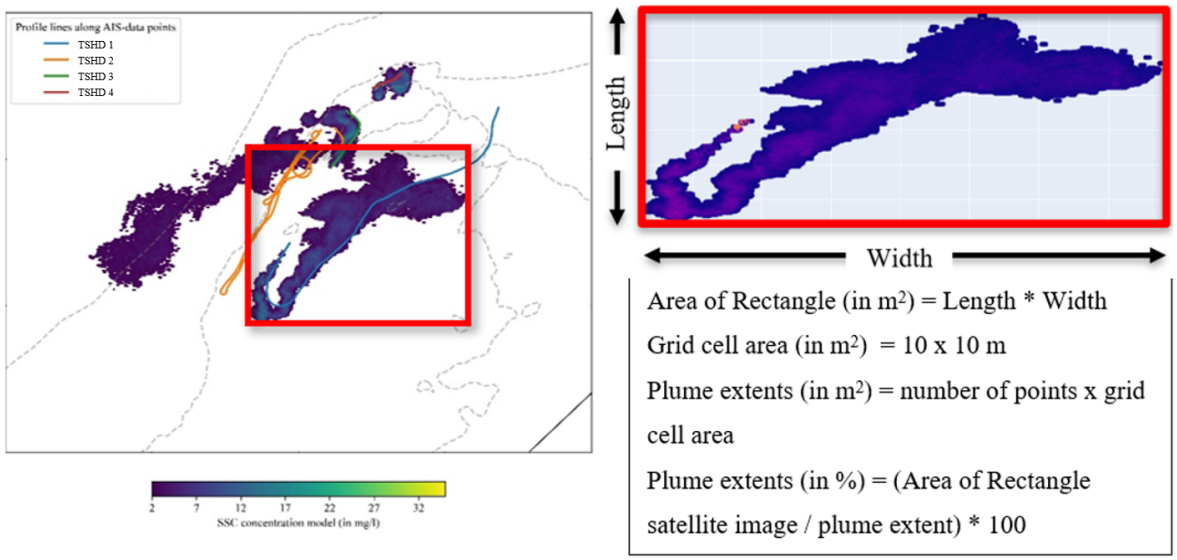

Figure 10: The following example illustrates the calculation of the area of a rectangle and plume extents in m^2 for the TSHD 1 sediment plume as observed in the satellite image dated 01/12/2022.

4.6 Sediment transport satellite based model set-up and validation

The sediment transport satellite based model (SB-model) of the study area was generated by the Delft3D Water Quality (DelWAQ) software, developed by Deltares. The software encompasses a comprehensive range of water quality parameters, thereby facilitating the modelling of sediment-water interactions (Deltares, 2024b).

4.6.1 Set-up of the sediment transport SB-model set-up and the Becker method

The hydrodynamic model generates DelWAQ outputs that describe the system's hydrodynamics. These DelWAQ outputs serve as the foundation for creating the sediment transport SB-model. Within the model, various parameters, such as output, simulation, and integration methods, were selected. It is crucial to note that the hydrodynamic model employs a different numbering system compared to the sediment transport SB-model. To aid in understanding these differences, Table 9 has been included.

Table 9: A z-σ layer comparison; the top layer differs for the ADCP, hydrodynamic, and sediment transport models.[3]

	ADCP	Hydrodynamic model	Sediment transport model
Top layer	n20	10	1
Bottom layer	n1	1	10

Table 10 summarizes the input parameters used in the DelWAQ model. These parameters were selected based on the model validation and sensitivity analysis. Of particular interest to the research questions are the fall velocity, source term and dispersion factor, which are described in further detail below.

[3] For clarity, the terms "top" and "bottom" layers instead of numerical identifiers were used in this document.

Table 10: Sediment transport DelWAQ parameters.

Parameter	Base settings
Runtime	05:35:00 hours
Grid aggregation	None
Hydrodynamic coupling interval	20 min
Time step	5 min
Solver	21.70
Horizontal dispersion factor	3 m^2/s
Amount of Sigma z-σ layers loads released	All layers
Fall velocity IM1	8.64 m/d = 0.1 mm/s
Fall velocity IM2	138.24 m/d = 1.6 mm/s
Critical shear stress for resuspension (erosion) of fluff layer	0.1 Pa
Critical shear stress for resuspension (erosion) of buffer layer	0.5 Pa
M0, zeroth-order resuspension flux	$1*10^{-3}$ $kg/m^2/s$
M1, first-order erosion velocity	1 s^{-1}
PsedMinIM	1.0 [-]

Fall velocity

In the process library of the sediment transport SB-model setup, it is possible to incorporate the sediment fractions IM1 and IM2:

- **Fraction IM1** refers to fine sediments that are easily picked up by the current and have a lower fall velocity. This can lead to surface plumes.
- **Fraction IM2** is the bulk sediment, which has a higher fall velocity and larger grain sizes.

The fractions were dispersed in the water column with specific loads and fall velocities. To clarify the relationship between the fractions and the percentage of fines, Figure 11 has been included. The percentage of fines carries significant uncertainty and can vary during dredging operations. The sediment transport SB-model can utilize multiple approaches, incorporating different amounts of IM fractions. Section 4.6.3 discusses the effects of these variations in detail.

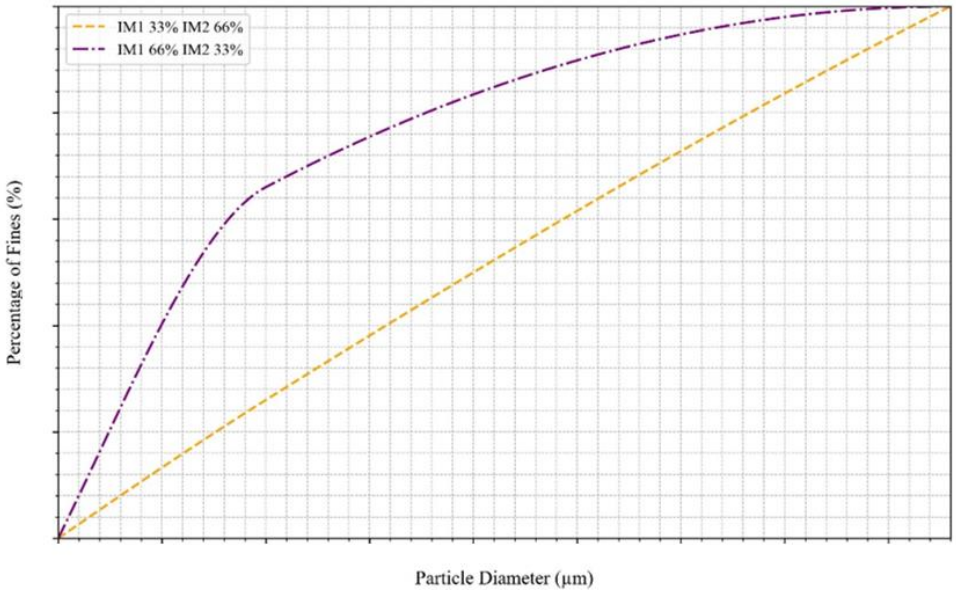

Figure 11: Percentage of fines plotted against the sediment diameter (of which the possibility 66% IM1 33% IM2 and 33% IM1 and 66% IM2 are plotted)[4].

The sediment transport SB-model utilizes two IM fractions because they offer practical advantages in terms of different sediment fall velocities. The sediment fall velocities were calculated using Stokes' formula. This formula allows the user to determine the velocity at which a sediment particle will fall based on the initial density and radius of the sediment particle and the fluid. The Stokes' formula (Equation 7) is as follows:

$$w = \frac{1}{18}\frac{g(s-1)d^2}{v}$$ Equation 7

[4] Percentage of fines is confidential.

With:

g = acceleration of gravity (m/s^2),

s = relative density ρ_s/ρ_f *(ρ_s = density of object (kg/m^3), ρ_f = density of the fluid (kg/m^3))*,

d = diameter of the Particle (m), and

v = kinematic viscosity in m^2/s (van Rijn, 2007).

Stokes' formula utilizes several key parameters (gravity (in m/s^2), relative density (in kg/m^3), particle diameter (in m), and kinematic viscosity (in m^2/s)) to calculate the fall velocity of particles. In the sediment transport SB-model, the particle diameter, dry density, and fall velocity from the PD-model were used, as shown in Table 11. Sensitivity analyses were conducted with various fall velocities, and it was concluded that the fall velocity from the PD-model provided the best fit.

Table 11: IM1 and IM2 fractions, floc size and resulting fall velocity in the unit months per day.

Sediment fraction	Particle diameter (in µm)	Fall velocity (in mm/s)	Fall velocity (in m/d)
IM1	10	0.1 mm/s	8.64 m/d
IM2	43	1.6 mm/s	138.24 m/d

Source terms

To define the source terms for the model, the Becker method, as described in Section 2.3, was employed. The source term caused by overflow was calculated using the code provided in Appendix E, which determines the sediment plume in the top layer. Additionally, this code includes a Monte Carlo analysis to calculate the source terms.

The Monte Carlo analysis serves as a valuable tool for simulating a range of potential scenarios and estimating the probability of different outcomes. This approach helps in creating a more realistic source term, especially when dealing with numerous uncertainties. The uncertainties covered are shown in Table 12.

Table 12: Uncertainty parameters Monte Carlo analysis[5].

	Fines	Rho dry (kg/m^3)	σ drag head	σ overflow	σ entrapment	σ settlement	σ far-field
P20	*	*	0.01	0.10	0.01	0	0.01
P50	*	*	0.02	0.15	0.03	0.10	0.05
P80	*	*	0.03	0.20	0.05	0.20	0.1

The Monte Carlo analysis generates a probability distribution of potential source terms for turbidity modelling, allowing for the assessment of uncertainty and variability in the source term. To reduce uncertainty in the calculations, vessel log files[6] were obtained when available for dredging cycle information (Example Figure 12).

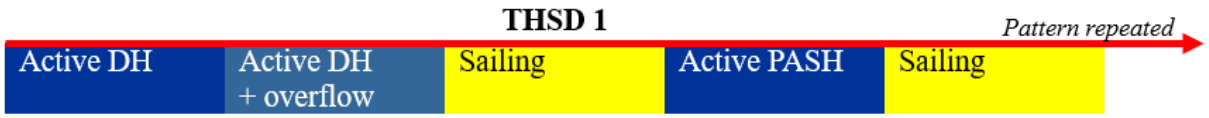

Figure 12: The dredging cycles of the TSHD 1 dredging cycle[7].

The incorporation of log file data enhances the precision of the calculated source term for the TSHD 1 and THSD 2, as compared to previous estimates. The calculated peak source term 80% exceedance values for satellite date 01/12/2022 are displayed in Table 13.

Table 13: Provides examples of TSHD 1 and 2 overflow peak source terms, specifically P20, P50, and P80, with their respective values in kg/s for January 12, 2022. Appendix C contains additional overflow values.

Vessel	P20	P50	P80
TSHD 1	85.9	104.6	125.8
TSHD 2	66.3	80.6	96.6

[5] Fines and Rho dry are confidential.

[6] Due to project confidentiality the vessel names were left out.

[7] The dredging cycle values were left out do to confidentiality.

In the absence of log data for some TSHDs, an estimate was derived by examining the log files of a comparable vessel engaged in dredging operations at the borrow area and analysing the AIS data point profile. Eventually, the peak source term 80% exceedance values displayed in Table 14 were used.

Table 14: Source term P80 values for each of the dredging vessels (TSHD 1 to 7) are presented in the satellite images before and after overflowing started. If only one value, then it means the overflowing a little.is estimated to start when dredging in smaller amounts. The **bold** represents the source term, and vessel used for the sensitivity analyses.

Satellite date	**Used source term**			
01/12/2022				
Vessel	**TSHD 1**	TSHD 3	TSHD 4	TSHD 2
Drag head Overflow	**670 1340** **4100 8200**	605 1210	750 1500 4660 9320	520 1040 3225 6450
01/17/2022				
Vessel	TSHD 5	TSHD 4	TSHD 6	
Drag head Overflow	680 1360 4225 8450	680 1365	420 840	
01/22/2022				
Vessel	TSHD 1	TSHD 4	TSHD 6	
Drag head Overflow	515 1030 3205 6410	570 1140	405 805 2515 5030	
03/28/2022				
Vessel	TSHD 1	TSHD 7		
Drag head Overflow	560 1120 3480 6960	570 1140 3550 7100		

The source terms for dredging operations can vary depending on the vessel and the date of the satellite image. This variation was due to differences in the dredging duration and the volume dredged, which can affect the input data. If the vessel has just started dredging in the satellite image, only the drag head peak source term was added as input.

Dispersion factor
The dispersion factor was adjusted in accordance with the recommended value range set forth by Deltares (Table 15). The following is a list of the most common ranges of horizontal dispersion terms in aggregated models with a finite grid (Deltares, 2024b). For this research was the range between 1 and 10 m^2/s investigated.

Table 15: The horizontal dispersion factor's common ranges for different mixing phenomena.

Mixing phenomena	D [m^2/s]
Molecular diffusion	1 x 10-9
Vertical diffusion (stratified systems)	1 x 10-4 – 1 x 10-6
Vertical diffusion (non-stratified systems)	1 x 10-1 – 1 x 10-3
Turbulent diffusion	0.1-1.0
Depth integration estuaries and seas	10 -1000
Tidal and depth integration estuaries and seas	100-1000
One dimensional river	100-1000

4.6.2 Validation of the sediment transport SB-model against satellite imagery

The sediment transport SB-model was validated against satellite imagery to assess the model's accuracy and precision. It is important to consider that the satellite imagery contains inherent uncertainties due to the algorithm used by WaterInsight to derive the TSS values (Section 3.4).

The validation process involved plotting a profile along the AIS trajectory with TSS values from both the sediment transport SB-model and the satellite imagery. From this profile, the RMSE, R^2, and bias of the TSS concentrations were calculated. Additionally, satellite image vs. observed values and a Bland-Altman plot were generated.

To verify differences not only along the profile, a difference layer from the model relative to the satellite imagery was created, zoomed in on the specific location. Furthermore, the RMSE, R^2, and bias were calculated for all models relative to the satellite image TSS concentrations (in mg/l) for the Plume area 1[8]. This comprehensive approach ensures the accuracy of the predicted plumes at the borrow area.

To quantitatively assess the size of the plume, the area of the rectangle and plume extents were calculated from both the satellite imagery and the model predictions. This analysis considered not only the total extent but also the far-field prediction relative to the near-field prediction of the sediment plume. Appendix E includes the code used to create the plots and calculate the analysis parameters.

[8] Plume area 1 coordinates are confidential.

4.6.3 Sensitivity analyses of sediment transport parameters

A sensitivity analysis was performed by adding the P20, P50, and P80 source term overflow values to the model, as well as changing the timestep, fall velocity, and dispersion factors. The changed values are added to Table 16.

Table 16: Sensitivity Analysis of Model Parameters and Values. The **bolt** text is the used model used.

Parameter	Value			
AIS timestep	**1 minute** 10 seconds			
Simulation and output timestep	**1 minute** 5 minutes 10 minutes		1 minute **5 minutes** 10 minutes	
Source term overflow parameters i.e. Percentile (P) exceedance peak values, layers applied and overflow starting point	**P20** P50 P80 Overflow source term from start dredging	**10 layers** “” “” Source term from start overflow	6 layers “” “” **Dredging source term until start overflow**	1 layer “” “”
Fall velocity input i.e. floc size, fraction size and proportion	**IM1 = 10 µm 66%** IM1 = 10 µm 33% IM1 = 10 µm 33% IM1 = 14 µm 33%	**IM2 = 43 µm 33%** IM2 = 43 µm 66% IM2 = 25 µm 33% IM2 = 28 µm 33%	IM3 = 43 µm 33% IM3 = 42 µm 33%	
Horizontal Dispersion Factor	**3 m^2/s** 1 m^2/s 10 m^2/s			

4.6.4 Planning and Design phase model (PD-model)

The PD-model was created to predict sediment dispersion on-site. The source terms used in the PD-model describe the initial conditions that were predicted for sediment dispersion when vessels from each project would dredge during a certain season, with differing scenarios. To test whether satellite imagery can indeed improve model predictions, a stationary model with a source term, dispersion coefficient, and fall velocity predicted in the planning and design phase was modelled.

The focus was on assessing how much the model improves using satellite imagery relative to the planning and design phase. The satellite images were all captured during the winter North East monsoon, a relatively dry period. The scenario was based on a model developed by an engineer in the planning and design phase. In this scenario, vessels from two projects were dredging simultaneously. The model inputs included a scenario of 4 TSHDs dredging at the same time, with the predicted source terms, dispersion coefficients, and fall velocities detailed in Table 17.

Table 17: PD-model input parameters for the source term, fall velocity and dispersion coefficient.

Equipment	Source term origin	Peak source term (in kg/s)		
TSHD (33000 m^3)	Drag head	13	18	24
	Overflow	81	102	124
Parameter		value		
IM1 fall velocity		8.64 m/d		
IM2 fall velocity		138.24 m/d		
Dispersion coefficient		1 m^2/s		

In this scenario, a total of 4 TSHDs were deployed, and different dredging cycles were used as input for the Becker calculations due to varying sailing distances from the borrow area to the project site.

5| RESULTS

5.1 Hydrodynamic model results

5.1.1 Hydrodynamic process description

In order to accurately represent the hydrodynamic conditions of the satellite images, it was necessary to understand the processes governing the hydrodynamics of the numerical model, which are described below.

Tidal influence

The amplitude of the tide changed slightly, by about 0.05 m, in the water level between monitoring stations S and C, but the difference in phase was still very small (Figure 13a). During low tide, the tide gauge was out of the water, as shown by flat surfaces (Figure 13b), which resulted in not being able to capture the low tide except for neap tides. The spring tide exhibited a tide height of about 1.2 m, while the neap tide was only about 0.3 m (Figure 13b). This resulted in a difference of 0.9 m between the neap and spring tides. As previously mentioned in Chapter 3.2.2, Figure 13 confirms that the tide consists of both semi-diurnal and diurnal tidal components (mixed diurnal tide).

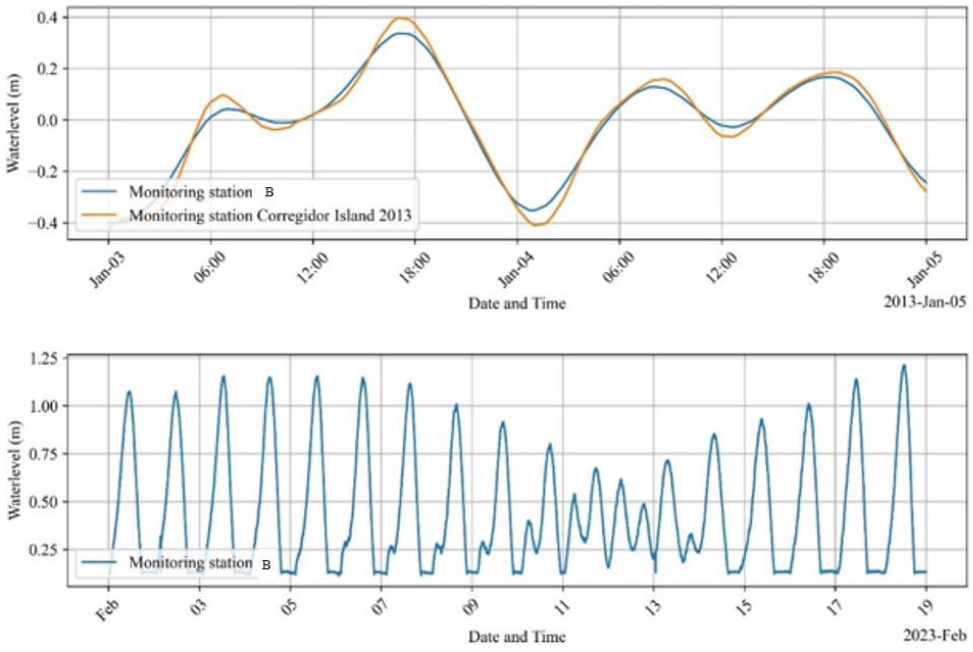

Figure 13: Water levels (in m) over time at monitoring stations B and Corregidor Island (monitoring station C) in January 2013 (upper panel) and at monitoring station B in February 2023 (bottom panel).

Current velocities

Figure 14 shows that the currents are the consequence of the movement of vast quantities of water towards or away from the Bay as the tide fluctuates. Tidal currents move inwards towards the Bay during high tide, when the water level rises between low and high tide. During ebb tide, the tidal currents move away from the Bay as the water level falls between high and low tide. The strongest tidal currents occur midway between ebb and flood as seen in the arrow magnitude of Figure 14b and c. A slack tide is defined as a period of no current, which can also be seen in Figure 14. When it is high tide at approximately 14:00 (Figure 14a), the current magnitude is around zero in Figure 14b. Slack tides occur when the flow of water changes direction between high and low tide (Seraphin, 2024).

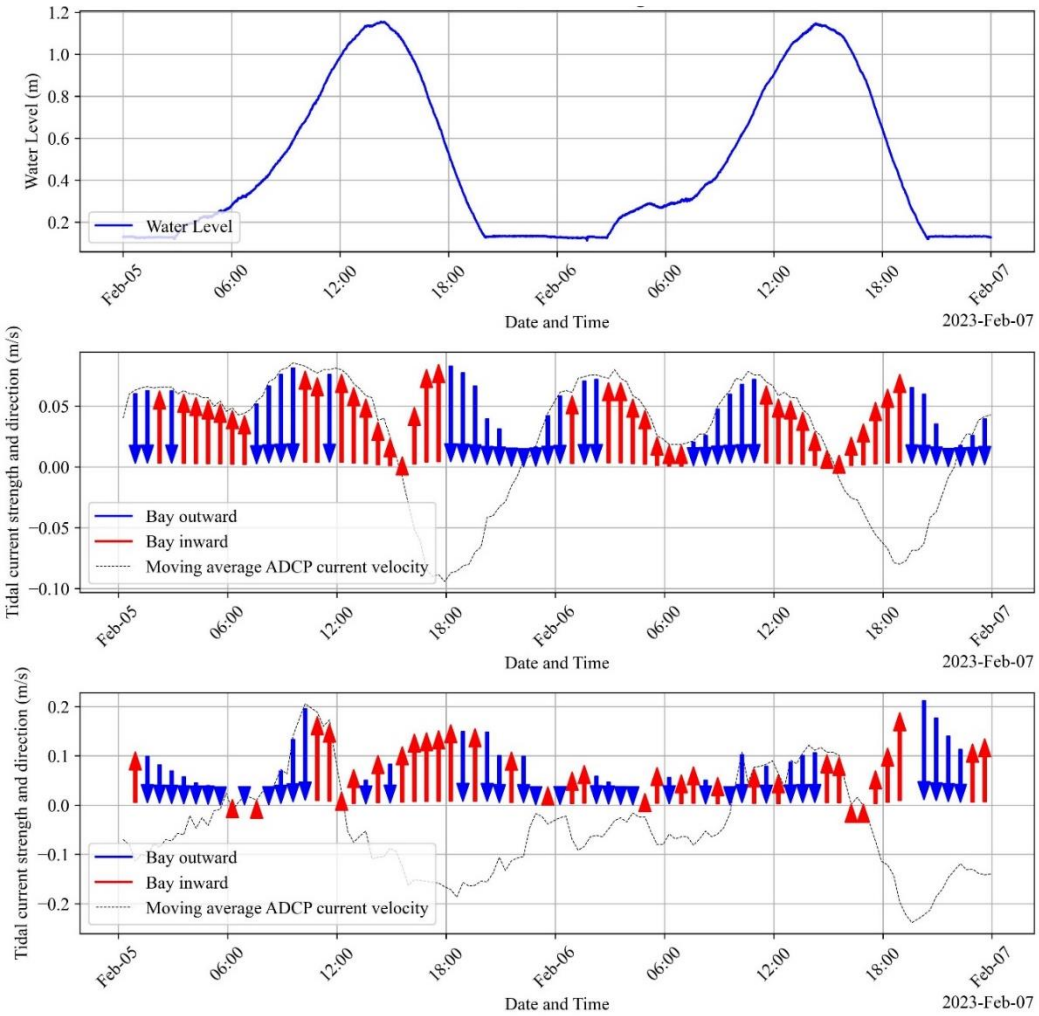

Figure 14: The height and strength of tidal currents in Manila Bay undergo a mixed diurnal tide variation. The length of the arrows indicates the strength of the tidal current.

The current velocity of top layers (n19) had considerable fluctuations, while the bottom layer (n1) displayed less variability (Figure 15). These observations indicated that hydrodynamic forces, such as wind, might have been influencing current velocity and direction in the top layers, but to a lesser extent in the bottom layers.

The average direction of the current in top layers (1 and 2) (≈225 degrees, 0.4 m/s) was almost opposite to that in top layers (19 and 20) (≈30 degrees, 0.5 m/s) in February 2023 (Figure 16).

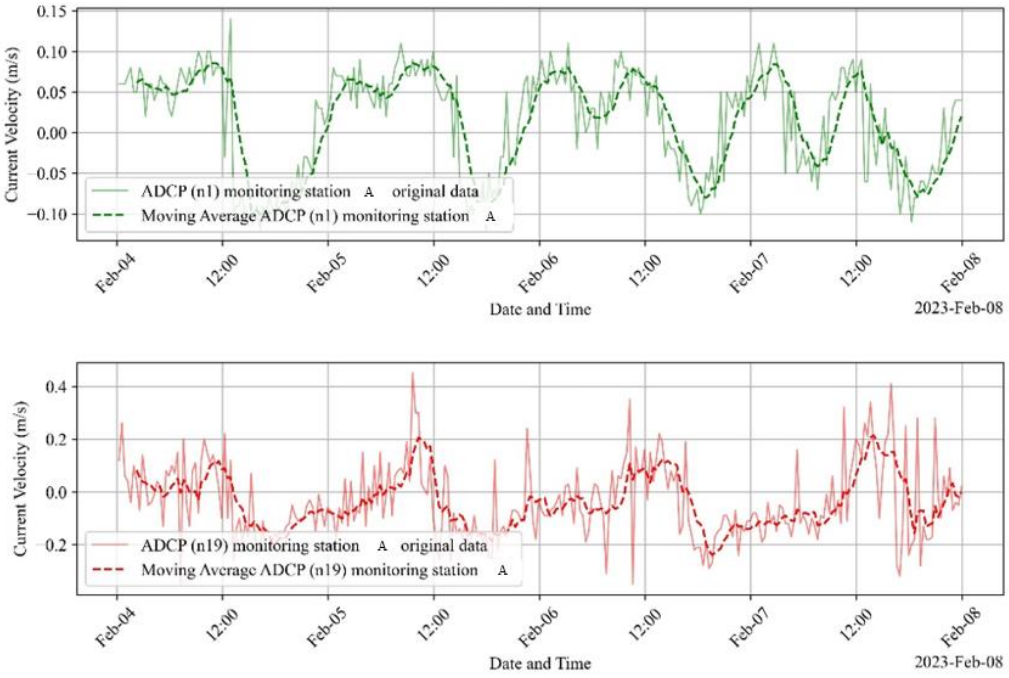

Figure 15: Two-line graphs n1 at the top and n19 below, each representing the current velocity measured by an Acoustic Doppler Current Profiler (ADCP) at Monitoring Station A over several days in February 2023. A positive velocity means that the direction is between 304 and 360 and zero and 124 degrees. Conversely, a negative current direction is indicated when it lies between 124 and 304 degrees.

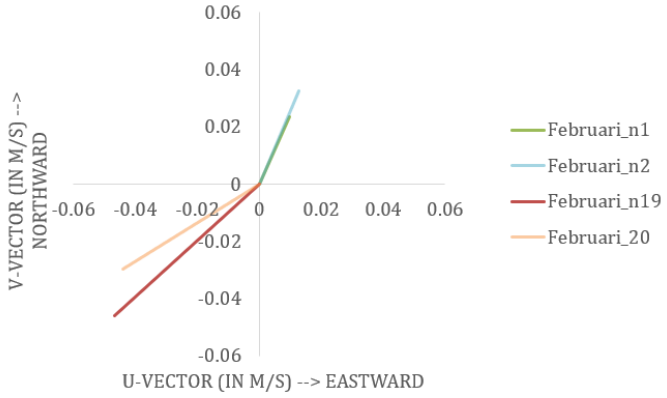

Figure 16: The data presented is over the course of the entire month of February 2023. The mean vector to the mean V components indicates the current's speed and direction. A positive value indicates an easterly or northerly direction. The axes are expressed in meters per second, showing the layers n1, n2, n19, and n20.

Prevailing wind

The changing direction of the residual wind vector observed in February and July 2023 was in agreement with the current of the ADCP at the top layer, indicating a direct dependence on wind direction for the top layers (Figure 17).

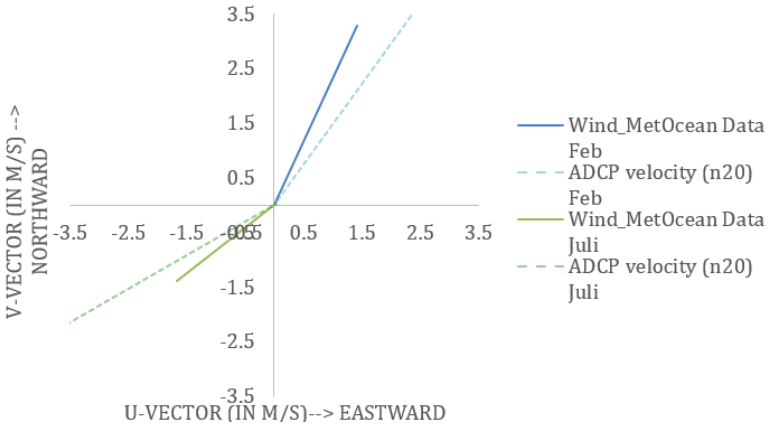

Figure 17: Wind data as residual wind vectors against the current residual vector of layer n20 for the period encompassing the months of February and July in the year 2023.

5.1.2 Hydrodynamic model validation against in-situ measurements

Validation of the hydrodynamic model was achieved through an examination of the analysis parameters for the top model layers, specifically layers 9 and 10, against layer 19 of the in-situ ADCP data (Table 18). The analysis parameters indicated minor differences between the model and the observed in-situ data because the RMSE and bias were near zero, which indicated the hydrodynamic model on average performed well in capturing velocity. However, the R^2 and correlation coefficient suggested that there were peaks or outliers that were not well captured. Based on these measurements, Layer 9 seemed to do a little better than Layer 10 in terms of how well the model matched up with real data (see Appendix A for more statistical analysis values). Furthermore, Layer 9 performed better in terms of stability and correlation with observed data, as it showed fewer outliers compared to Layer 10 (Figure 18).

Table 18: RMSE, R^2, BIAS and correlation for velocity. With RMSE and BIAS in m/s, the R^2 and correlation were dimensionless.

Analysis parameter	Layer 9	Layer 10
RMSE (Moving Average in m/s):	0.08	0.08
R^2 (Moving Average):	0.32	0.31
BIAS (in m/s):	0.003	-0.009
Correlation between 'model(FlowFM)' and 'Observed(In-situ data Moving Average)':	0.57	0.57

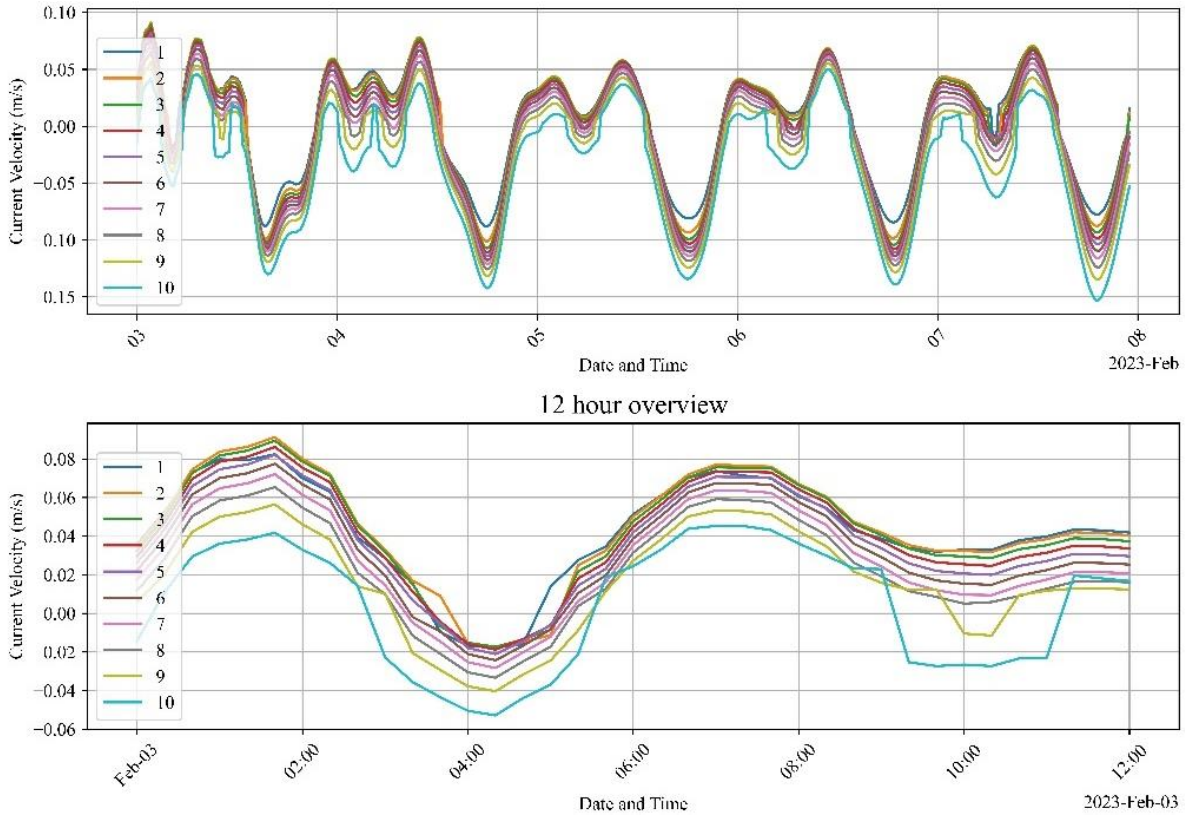

Figure 18: Current velocity at z-σ layers 1–10, with 1 being the bottom layer and 10 the top layer. The displayed data in the upper panel is from the 3rd of February, 2023, to the 8th of February, 2023. The lower panel presents a 12-hour overview of the 3rd of February with a zoom-in feature. The data set encompasses the period from 00:00 to 12:00 in 2023.

A fluctuating pattern with peaks and troughs indicated a variability in the current velocity over the observation period (Figure 19). The modelled and observed velocities showed a similar trend, indicating that the model captured the observed current velocity behaviour with reasonable accuracy. However, there were instances where the lines diverged, suggesting that there were discrepancies between the model predictions and the actual observations.

Consequently, while the RMSE and BIAS were satisfactory, the R^2 was not. Since the higher peaks were normally represented in the model, this implied that the model would likely be effective in defining residual transport but not extreme events (Figure 19). In conclusion, the overall trend and positioning of the troughs and crests were well captured, but the peaks would be underestimated. These underestimated peaks could influence the sediment transport model sediment plume in terms of dispersion and main direction behaviour. Nevertheless, the general hydrodynamics dominating sediment dispersion were well captured and gave confidence that the hydrodynamic model was sufficiently accurate to proceed with calibration of the sediment transport model against satellite imagery.

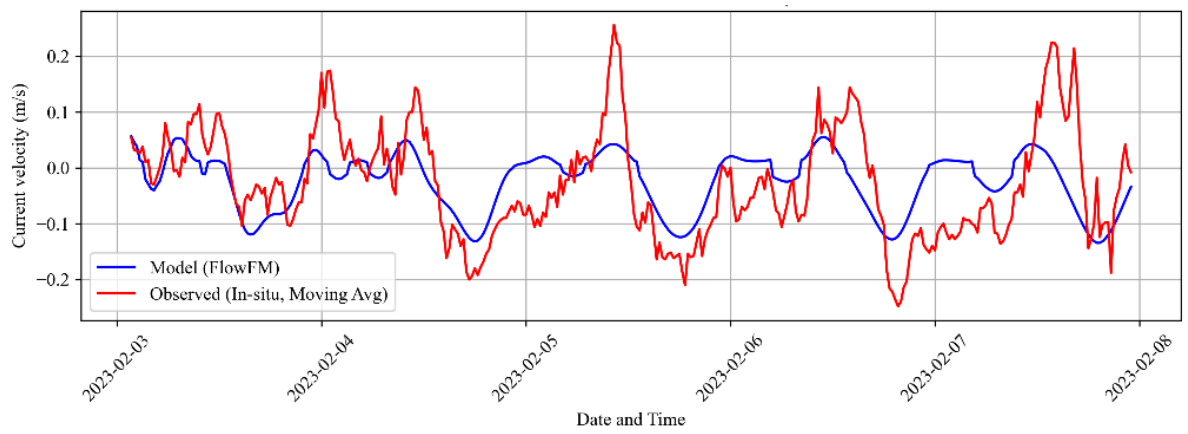

Figure 19: Model (Layer 9) vs. Observed (Layer n19) data at position A near the borrow area. The model is shown in blue, and the observed ADCP is shown in red.

A correlation of 0.57 indicated a moderate positive correlation, which can be interpreted as follows: as the predicted values increased, the observed values also tended to increase. This indicated that the model was able to capture the general trend of the data, although the relationship was not perfect. A comparison between the two variables was shown in the scatter plot (in Figure 20, left panel). The trend line indicated that there was a positive correlation between the model and the observed data. However, the dispersion around the trend was high.

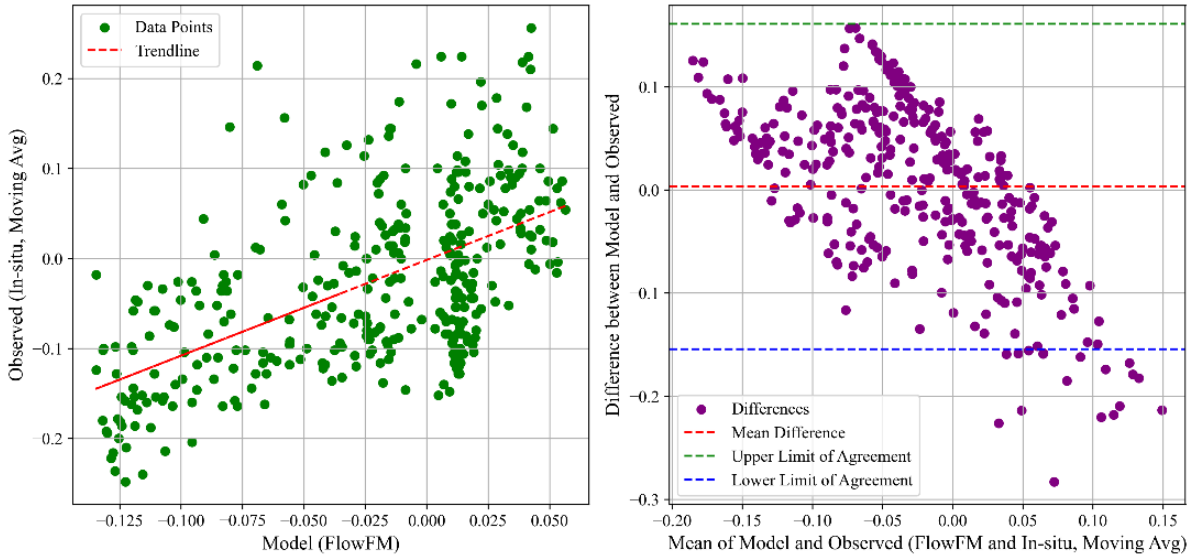

Figure 20: Comparison of the outputs from a model (x-axis) to observed data (y-axis) (left panel) and assessment of the agreement between the two different measurements (right panel). On the right, the x-axis displays the mean of the model and observed values, while the y-axis depicts the difference between the model and observed values. The purple dots represent the differences for each paired measurement. The red dashed line shows the mean difference, and the green and blue dashed lines show the upper and lower limits of agreement, respectively.

The Bland-Altman plot showed that most of the data points were within acceptable limits of agreement, although there was a small average bias in the model predictions (Figure 20, right panel). Overall, while the model performed adequately, there is room for enhancement to better capture the variability in the observed data and improve the predictive accuracy. However, it was considered sufficient in capturing the general trend of the current velocity magnitude and direction, the key variables of the hydrodynamic model that govern sediment dispersion.

Numerical parameters

According to the analysis, grid independence for the hydrodynamic model appeared to be around 130 by 130 m, reducing the calculation time without affecting the accuracy of the results relative to a 65 by 65 m grid size (Figure 21). The 260 by 260 m grid reduced the time required for calculation by 4 hours and 15 minutes relative to the calibrated scenario (which took approximately 5 hours) but also significantly degraded performance. The 260*260 m scenario exhibited an RMSE of 0.20 m/s and a negative R^2 value relative to the calibrated scenario, indicating a lack of predictive accuracy. The larger grid size had a significant negative impact on the model's performance and could lead to substantial inaccuracies. Nonetheless, it was important to consider the plume size when selecting the grid size for the borrow area. Given that the satellite images have a resolution between 10 and 60 m, the 65 by 65 m grid size was used for the hydrodynamic model.

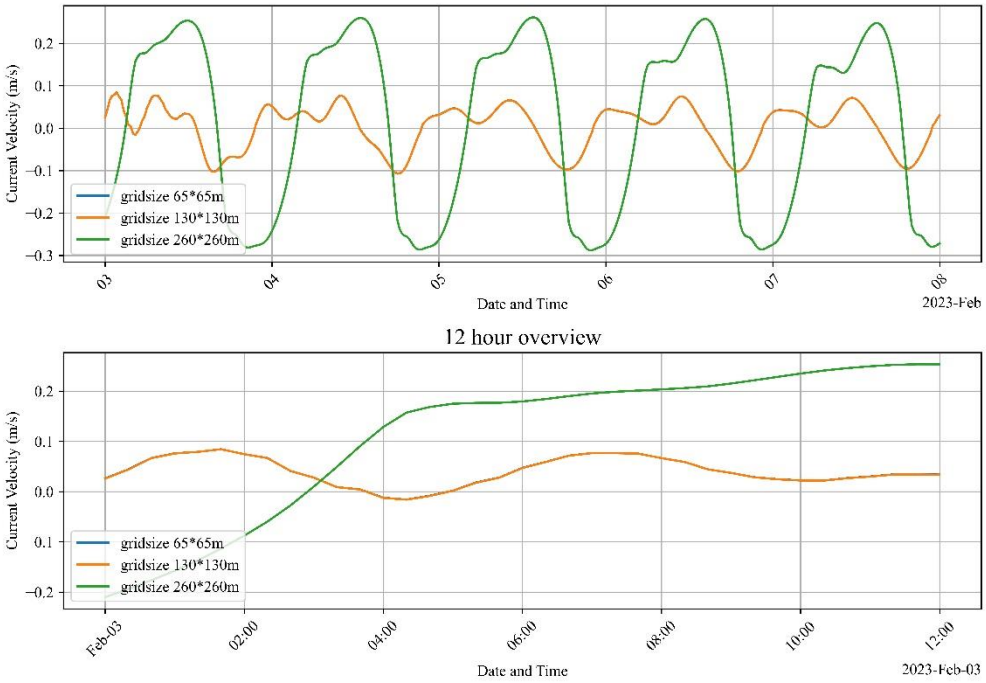

Figure 21: Different grid sizes and their effect on current speed: negative values flow offshore and positive values flow inwards. The orange and the blue lines are coincident, reason why the blue line cannot be seen in the figure.

Upon examination of the analysis values, it was evident that the increase in the Courant number to 0.9 had no effect on the accuracy of the model when it was below 1. The distribution of the Courant number remained stable during the simulation. The calculation time, however, was approximately six hours longer.

Modifying the maximum timestep to 60 seconds from 30 seconds resulted in a reduction in calculation time of approximately 15 minutes, accompanied by a slight increase in the root mean square error (RMSE), yet maintaining near identical accuracy. The maximal timestep had no impact on the model's representation, but it did result in an approximately 7-hour and 39-minute increase in calculation time. The reduction of sigma z-σ layers to five layers resulted in a minimal increase in RMSE and a slight BIAS while maintaining nearly perfect accuracy and a reduction in calculation time of approximately one hour and 15 minutes. Reducing the number of z-σ layers had a slight impact on accuracy, but it also improved efficiency (Table 19). However, 10 z-σ layers were chosen because the top layer represented 4% of the depth which was equal to 1 m in a 25-m depth water column. The TSS concentration layer thickness from the satellite image was unknown, but estimated at 1 m at the outer boundaries of the sediment plume. Therefore, 10 z-σ layers were selected for better comparison between the model and the satellite image derived TSS concentrations.

Table 19: Numerical parameter sensitivity analyses, calibrated scenario (Table 7) vs. different numerical parameters. With RMSE and BIAS in m/s, the R2 and correlation are dimensionless (for velocity).

Scenario	RMSE (in m/s)	R^2	BIAS (in m/s)	Calculation time HH:mm:ss
02_130*130 m grid	0.00	1.00	0.000	03:07:00
03_260*260 m grid	0.20	-13.39	0.006	01:43:00
04_courant number 0.9	0.00	1.00	0.000	10:57:00
05_maximum timestep 60s	0.00	0.99	0.000	04:47:00
06_max_timestep_5s	0.00	1.00	0.000	12:39:00
07_z-σ layers_5	0.00	0.99	0.000	03:42:00

In conclusion, it managed to produce a robust model that was independent of its nonphysical parameters.

Hydrodynamic parameters

The introduction of wind, whether with average in-situ or ISA density and pressure (Table 7), resulted in a reduction of the R^2 and an increase of the RMSE and BIAS. This suggested that integrating wind pressure and density into the model leads to a decline in model performance in comparison to a scenario in which wind was absent. The incorporation of these factors introduces complexity and potential limitations to the model's capacity to accurately capture wind effects (Table 20 and Figure 22). However, both scenarios involving wind input demonstrated a high impact on the model relative to numerical parameters, indicating that wind input had a notable impact on the model's results. The incorporation of wind resulted in a reduction of the model's accuracy in comparison with scenarios without wind input. This suggested that wind was an influencing factor in the model results and should be given consideration when setting up the model.

Table 20: Model sensitivity to the addition of wind and a variable wind density and pressure.

Scenario	RMSE (in m/s)	R^2	BIAS (in m/s)
08 wind in-situ density(1.225) pressure(101350)	0.026	0.753	-0.025
09 wind ISA density and pressure	0.027	0.736	-0.026

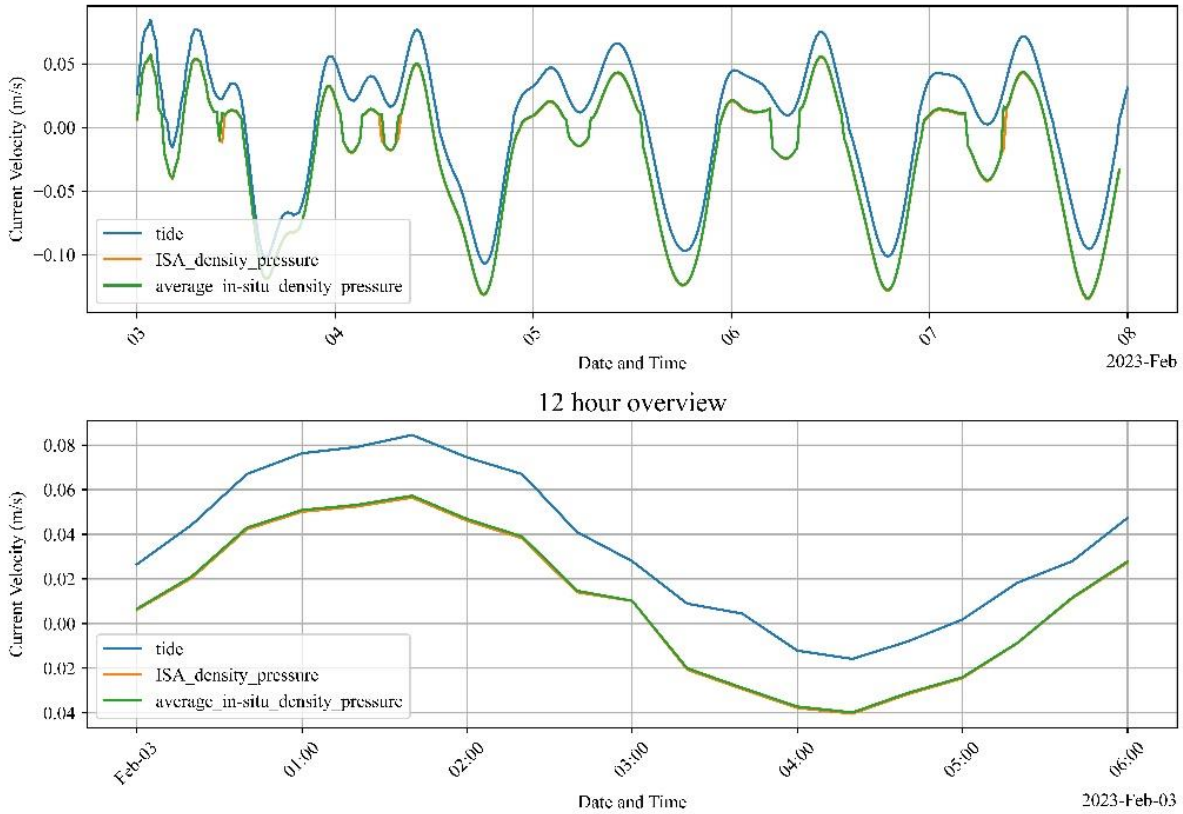

Figure 22: The model output with solely tidal input is presented for comparison with the model output with both wind and tidal input, as well as differing pressure and density. It can be observed that the results obtained with the ISA density and pressure are practically coincident with the results from the average in-situ density and pressure.

A robust numerical model was established with good non-physical parameters. As a result, it was expected that the model was sensitive to hydrodynamic parameters such as wind. Changes in grid size, Courant number, timestep, and z-σ layers had less of an effect on accuracy (RMSE and R^2) than changes in wind input. This underscored the significance of wind input in the model. In conclusion, the model was mostly tidal-driven, but one should not forget the significance of the wind for model hydrodynamics.

5.2 Satellite imagery

Four satellite images were selected for further analysis from the set of satellite images with TSS concentration values processed by WaterInsight. The dredging vessels, that were actively dredging during or just before the satellite images were identified. After identification, the satellite images were analysed with respect to the plume AIS vessel track. The analysis revealed that background TSS concentration values differed per situation and that the relative current velocity was more challenging to distinguish than initially expected.

The satellite images (01/12/2022, 01/17/2022, 01/22/2022 and 03/28/2022) displayed prominent plumes, but the background values differed (Figure 23). For example, on the 17th the background values were higher than those on the 12th of January. On the 12th, the background values ranged from 0 to 3 mg/l, while on the 17th, the satellite image had background values ranging from 0 to 5 mg/l Figure 23. This difference was partly attributed to a larger discharge from the Pasig River.

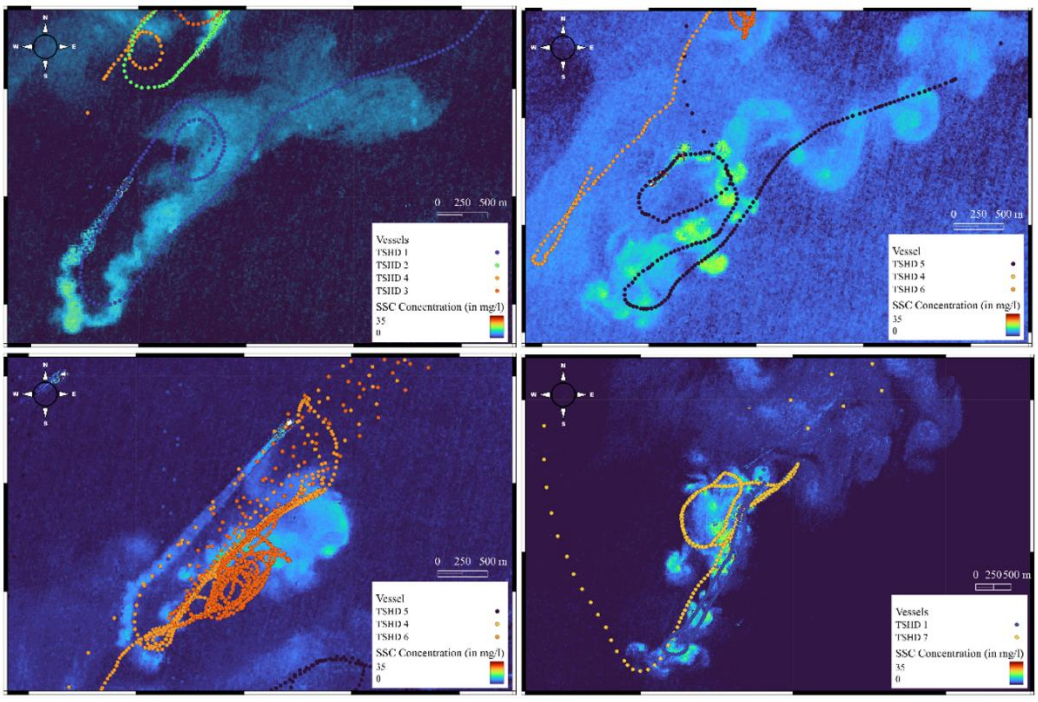

Figure 23: Some of the sediment plumes from the chosen satellite images with AIS-vessel tracks. Top left shows 01/12/2022 TSHD 1, top right 01/17/2022 TSHD 5, bottom left 01/22/2022 TSHD 4 and bottom right 03/28/2022 TSHD 1 and TSHD 7.

Due to variations in TSS background concentrations, plumes in some satellite images, such as the one from 01/17/2022, were challenging to analyse, and to provide a distinction between dredged and river plumes became challenging to distinguish. The background concentrations for each satellite image are shown in Table 21. Additionally, it was observed that during ebb tide, the plume moved offshore, whereas during flood tide, the plume moved inward into the Bay.

Table 21: The satellite image tidal state, height difference between high and low tide, current direction relative velocity to the AIS vessel track, and background TSS concentration values**.**

Satellite image	Tide (hours (h))	Tide decline (in m)	Current dir. (in degrees)	Relative vel. (in m/s)	Background value (in mg/l)
01/12/2022	1 h after low-tide	-0.18 +0.32	South-west 245°	0.13	2.5
01/17/2022[9]	2.5 h after low-tide	<-0.3 +0.75	South-west 250°	*	5.5
01/22/2022	0.5 h before low-tide	<-0.22 +0.78	North-east 85°	0.12	2
03/28/2022	8 h before high-tide	<0.3 +0.59	North-east 70°	0.04	1

The tides influenced the currents, and so they were included in Table 22 to determine the correlation between tide and current. However, to achieve a more precise correlation, further data was required. In Figure 23, the current direction is shown with red arrows.

The maximum concentration depended on the number of vessels dredging at the same location simultaneously. For example, in the satellite image from 03/28/2022, two vessels were dredging, the maximum concentration was higher compared to the image from 01/12/2022, where only one vessel was dredging.

[9] It was difficult to distinguish the relative velocity for satellite image date 01/17/2022.

The plume extents and maximum TSS concentration values differ per vessel and were included in Table 22. These values were influenced by several factors, including:

- The size of the dredging vessels,
- The duration of the dredging operation,
- The phase of the tide,
- The current velocity.

Table 22: Plume extent (in m^2), Area of Rectangle (in m^2) and maximum concentration of the sediment plume (in mg/l).

	Plume extent (in m^2)	Area of Rectangle (in m^2)	Maximum value (in mg/l)
01/12/2022 TSHD 1	3040600	13556752.2	17.6
01/12/2022 THSD 2	253700	521117.5831	17.7
01/12/2022 TSHD 3	461200	1123655.158	18.7
01/12/2022 TSHD 4	2230100	14062471.09	9
01/17/2022 TSHD 5	2710900	20769884	25.2
01/17/2022 TSHD 4	610200	2873939	21.3
01/22/2022 TSHD 1[10]	*	*	16.8
01/22/2022 THSD 6 & 4	1572000	5566053	13.8
03/28/2022 TSHD 1 & 7	8071600	30243379	32.3

In conclusion, a significant amount of information could be gathered from satellite images by analysing the data. Background values could influence the distinguishability of the plume extents and the Area of the Rectangle. Tide influences the current direction, and the relative velocity was challenging to calculate solely based on AIS vessel track data and satellite images.

[10] TSHD 1 Background TSS concentrations were difficult to distinguish from the plume, therefore the plume extent and Area of Rectangle of TSHD 1 were not included.

5.3 Sediment transport SB-model results

5.3.1 Sediment transport SB-model validation against satellite data

The sediment transport SB-model was calibrated by optimizing the input parameters until the sediment transport SB-model had the best accuracy relative to the satellite imagery. The validation of sediment transport SB-models was carried out by comparing simulations with satellite images, highlighting similarities and differences in plume predictions. Initial observations suggested that models generally predicted smaller plumes with higher near-field concentrations, although the plume shapes were similar (Figure 24).

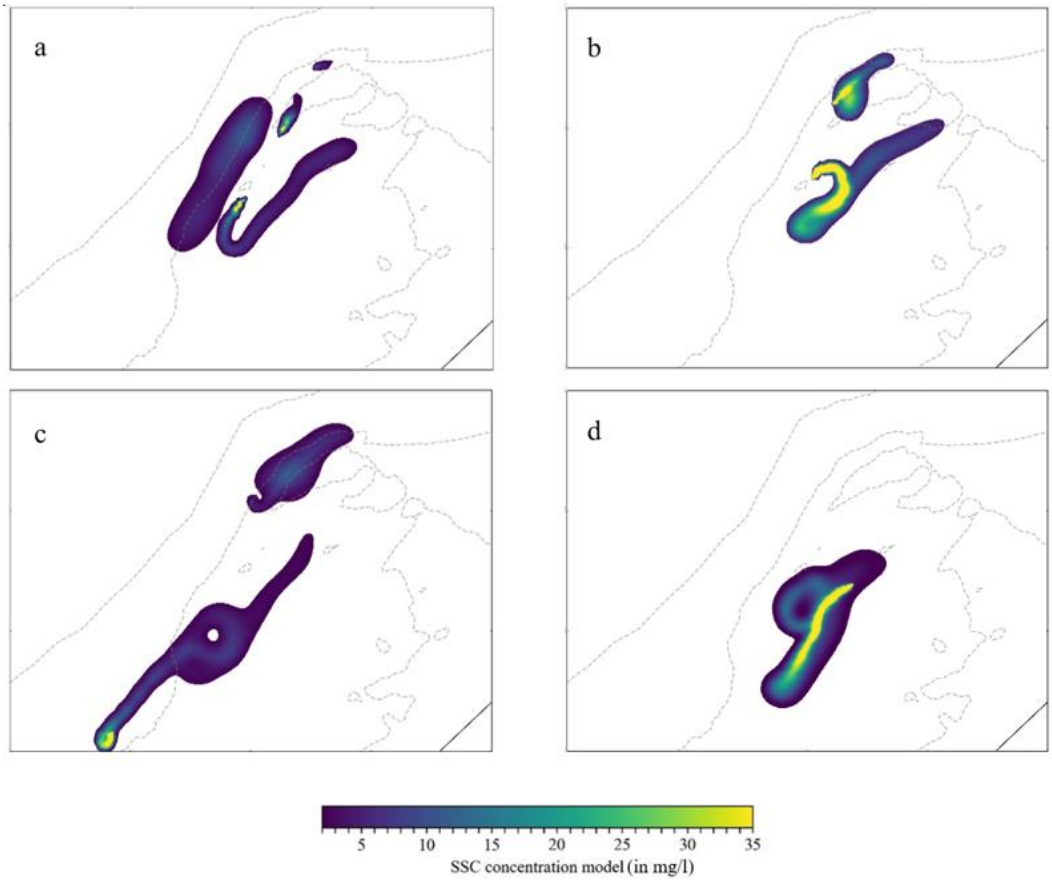

Figure 24: Model outputs for each satellite date with their TSS concentration above the background concentration (Table 22) , top left shows 01/12/2022, top right 01/17/2022, bottom left 01/22/2022, bottom right 03/28/2022.

A more in depth analysis was made by computing the Area of Rectangle, plume extents, and the percentage of the plume within the Area of Rectangle of the satellite image against the sediment transport SB-model. The plume extent area was found to be both under- and overestimated in the different satellite image date model simulations. Notably, TSHD 5 on

01/17/2022 showed the best modelling result in terms of plume extents, with a difference of 0.6%. Other plumes still exhibited significant differences in plume extents. For example, TSHD 2 had a plume extent difference of 35.7%, likely due to the short dredging time when the satellite image was taken (Table 23).

Table 23: Area of Rectangle (in m^2), plume extent (in m^2), plume extent (in %) The plume extent % is derived from the satellite image Area of Rectangle (in m^2) and the SB-model plume extent (in m^2).

Plume	Area of Rectangle model (in m^2)	Plume extent (in m^2)	Plume extent (in %) (SB)	Plume extent (in %) satellite image
20220112_TSHD 1	8337824	1985750	14.6	22.4
20220112_TSHD 2	64305	67600	13.0	48.7
20220112_TSHD 3	458187	232375	20.7	41.0
20220112_TSHD 4	8434037	3396900	24.2	15.9
20220117_TSHD 5	9825772	2830750	13.6	13.1
20220117_TSHD 4 & 6	1540041	566150	19.7	21.2
20220122_TSHD 4	4723234	2239250	40.2	28.2
20220122_TSHD 1[11]	28467067	6460025	*	*
20220328_TSHD 1 & 7	10267161	4909450	16.2	26.7

The profile line along the AIS data points track of each vessel was also analysed. Profiles with the best and worst fit were illustrated in Figure 25, with additional profile lines available in Appendix C. Models face challenges when vessels cross their own tracks, leading to overestimation of TSS concentrations. Overestimations were also observed in the near-field due to modelling difficulties, while far-field estimates (considered 2 km from the source) were more accurate.

The profile of the TSHD 1 (01/12/2022) showed maximum overflow at 5.8 km from the source (vessel), which was also reflected in the satellite image as the plume extent. Closer to the

[11] Unclear background TSS concentration data from satellite image.

source, the plume became smaller and fluctuated more (Figure 25). The model struggled to replicate the peaks of the plume in the satellite image from the source to approximately 3 km from it. TSHD 5 (01/17/2022) exhibited significant uncertainty in the near field of the plume until approximately 2 km from the source (Figure 25). This uncertainty could have been due to vessel speed and turning, causing the plume to react differently in the model compared to the satellite image.

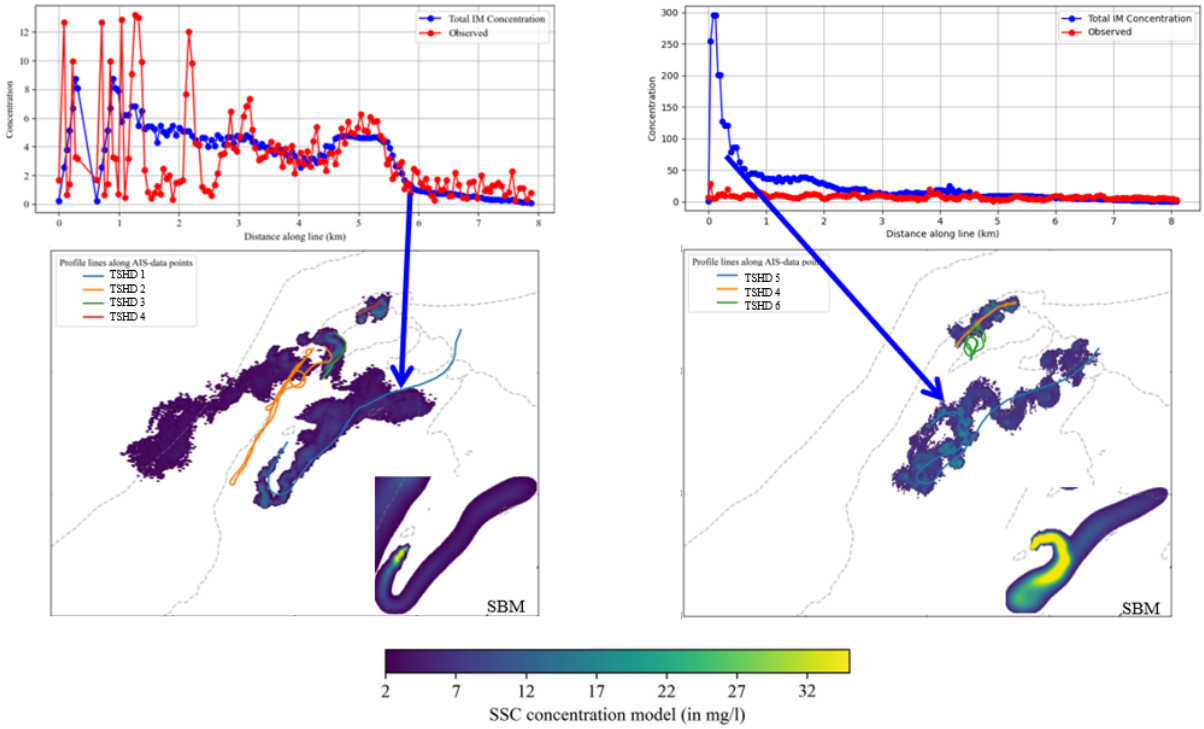

Figure 25: The AIS-vessel track TSS plume concentrations vs the distance for TSHD 1 01/12/2022 on the top left and TSHD 5 01/17/2022 on the top right. Corresponding satellite image TSS concentration (in mg/l) values without background values on the bottom. The blue arrows indicate the start of extensive overflow on the left and the position of too high concentrations on the right.

To assess the difference in position and concentration of the plume a difference plot per satellite date was produced (Figure 26). From the difference plots it can be concluded that the satellite plume was westward located in relation to the hydrodynamic model, indicating an error in the model hydrodynamics. This can particularly be seen in the difference plot of satellite date 01/12/2022 for the sediment plume of TSHD 4 (Figure 26). The concentration difference was the highest close to the vessel and when the vessel turned. This was not unexpected because it was known that the sediment prediction models had difficulty in the near field, that there was uncertainties in the hydrodynamic model and the higher concentrations in the turns was also expected. In a turn the vessel has more thruster water which would cause more sediments to spread in the top layer of the water column.

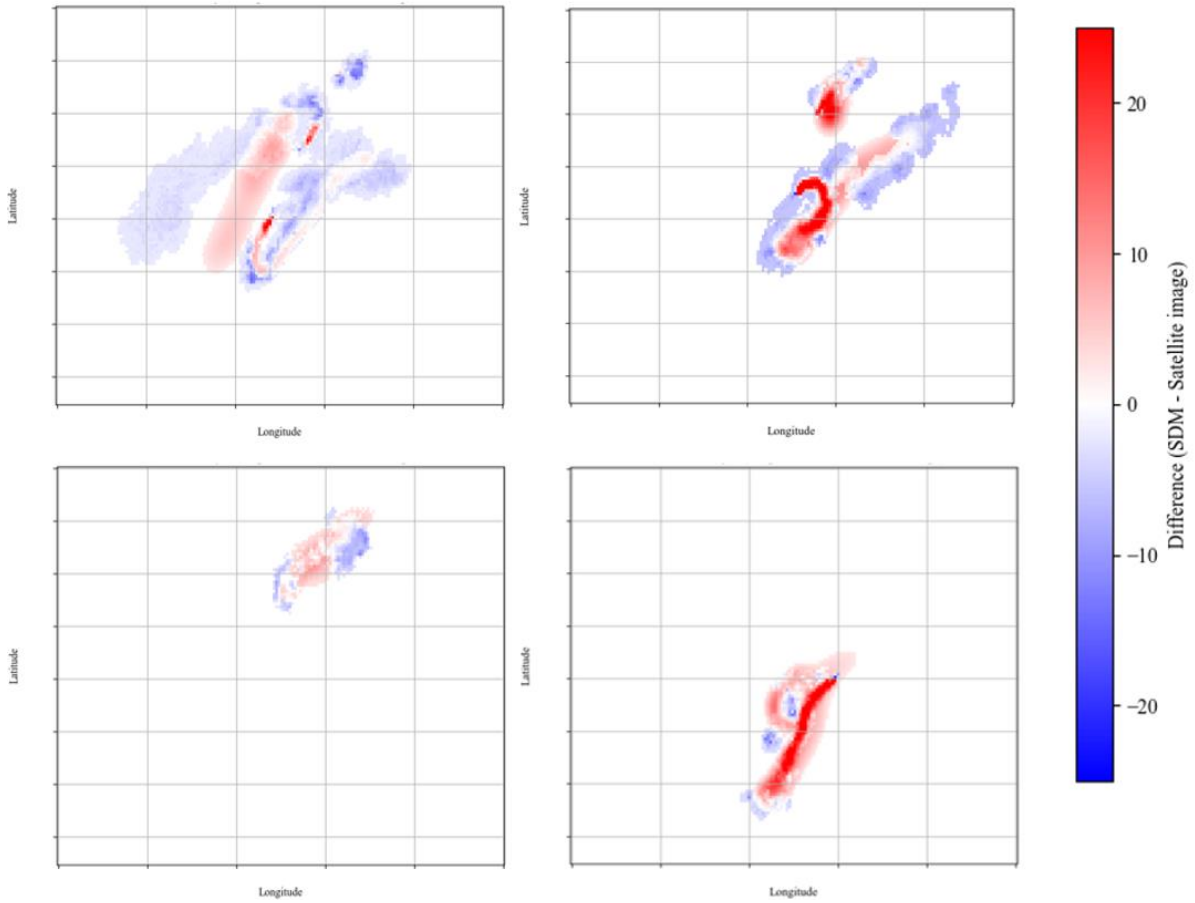

Figure 26: Spatial representation of the difference between model derived and satellite derived concentrations (in mg/m^3) for each satellite image date. On the top left is 01/12/2022, top right 01/17/2022, bottom left 01/22/2022 and bottom right 03/28/2022.

Finally, uncertainties of the model relative to Plume area 1 were calculated. This area was used to compute parameters such as RMSE, R^2, and bias of the predicted plume concentrations versus satellite-derived plume concentrations (TSS in mg/l). The results of this comparison were summarized in Table 24. The analysis of satellite imagery versus model-derived sediment plumes revealed varying performance across different dates. The lowest RMSE of 0.8 mg/l on 2022/01/22 indicated the closest match between satellite imagery and model predictions, while the highest R^2 of 0.44 on 2022/03/28 suggested the model best explained the variance observed in the satellite data. Conversely, the highest RMSE of 4.0 mg/l on 2022/01/17 indicated significant discrepancies, and the lowest R^2 of 0.13 on 2022/01/12 showed the model poorly predicted the observed sediment plumes. Overall, the data from 2022/01/22 represented the most accurate alignment with low RMSE and minimal BIAS, but a moderate R^2, suggesting a balanced yet improvable model fit.

Table 24: RMSE, BIAS and R^2 of the satellite image TSS concentration (in mg/l) values vs the sediment transport SB-model.

	RMSE (in mg/l)	BIAS (in mg/l)	R^2
01/12/2022	1.6	-0.06	0.13
01/12/2022	4.0	0.20	0. 31
01/22/2022	0.9	0.01	0.30
03/28/2022	3.5	0.37	0.45

5.3.2 Sensitivity analysis of the sediment transport SB-model

For the sensitivity analysis, the satellite image of 01/12/2022 with TSHD was used. The aim of the sensitivity analysis was to evaluate the influence of different scenarios on key performance metrics, such as area, width, and length, and their respective discrepancies from the PD-model. The scenarios explored included different horizontal dispersion levels, combinations of IM sediment fractions, and various z-σ layer configurations. Additionally, the influence of adding overflow load from the start of overflowing and dredging activities was assessed. Some of the metrics that were looked at are adjusted R^2, RMSE, bias, and plume extents %. This gave a full picture of how each scenario performed.

The sensitivity analysis demonstrated considerable variability in the plume area of TSHD 1, in plume extents %. To illustrate, Scenario 14 demonstrated a notable positive discrepancy in plume extent (+ 13 %) in comparison to the satellite image plume extent, whereas Scenario 8 exhibited the most negative considerable discrepancy in plume extent (- 19.2 %). See Table 25 for the other values.

Table 25: Plume extent total values and differences relative to the calibrated scenario.

	File	Area of Rectangle (in m^2)	Plume extent (in m^2)	Plume extent (in %)
0	Satellite image	13023815	3096500	23.8
1	Calibrated scenario	8258441	2873020	22.1
2	Horizontal dispersion 1	7982806	2505678	19.2
3	Horizontal dispersion 10	7791433	2950688	22.7
4	IM1	9145467	3160653	24.3
5	IM1 66% IM2 33% 10 43	9309580	3332312	25.6
6	IM1 IM2 IM3 10 25 43	8636171	3099639	23.8
7	IM1 IM2 IM3 14 28 42	8405687	2989399	23.0
8	P20 10 z-σ layers	841364	593791	4.6
9	P50 10 z-σ layers	8012223	2787308	34.8
10	P20 6 z-σ layers	8157370	2832219	21.7
11	P50 6 z-σ layers	8481485	3040396	23.3
12	P80 6 z-σ layers	8614759	3185339	24.5
13	Add overflow load from start overflowing	8086110	2791424	21.4
14	Add overflow load from start dredging	16133866	4787851	36.8

In terms of statistical performance metrics, the adjusted R^2 values ranged from 0.06 (Scenario 14) to 0.32 (Scenario 8), indicating a variation in the level of model fit. The RMSE values, which quantify the discrepancy between the observed and predicted values, showed considerable variation. The lowest RMSE was observed for Scenario 10 (0.98 mg/l), while the highest RMSE was recorded for Scenario 12 (1.43 mg/l). The bias was found to be consistently around 0 mg/l for all scenarios, indicating that there was approximately no systematic error in the predictions (Table 26).

The calibrated scenario is chosen because it provides a balanced performance across all three metrics, ensuring a good fit, low error and low bias compared to the other scenarios. While there are other scenarios with slightly better fits, the calibrated scenario provides a good overall compromise.

Table 26: R^2, RMSE, and BIAS values for the tests used for the sensitivity analysis relative to the used model.

	File Name	Adj. R-squared	RMSE (in mg/l)	Bias (in mg/l)
1	Calibrated scenario	0.23	1.05	-0.11
2	Horizontal dispersion 1	0.17	1.23	-0.11
3	Horizontal dispersion 10	0.22	0.98	-0.13
4	IM1	0.26	1.2	-0.06
5	IM1 66% IM2 33% 10 43	0.32	1.22	-0.02
6	IM1 IM2 IM3 10 25 43	0.27	1.14	-0.07
7	IM1 IM2 IM3 14 28 42	0.24	1.12	-0.09
8	P20 10 z-σ layers	0.06	1.1	-0.19
9	P50 10 z-σ layers	0.14	1.09	-0.14
10	P20 6 z-σ layers	0.22	1.11	-0.10
11	P50 6 z-σ layers	0.23	1.25	-0.07
12	P80 6 z-σ layers	0.24	1.43	-0.03
13	Add overflow load from start overflowing	0.22	1.05	-0.11
14	Add overflow load from start dredging	0.20	1.13	-0.06

5.3.3 Project and design phase (PD-) model vs satellite image

The PD-model was run with the same hydrodynamic framework as the sediment transport SB-model. Only the simulation time, source term, and dispersion factor, as elaborated in section 4.6.4 were adjusted. The PD-model was simulated over a time extent of 5 days with the specified TSHD dredging cycles. At first glance, the PD-model demonstrated big plumes with high concentrations at the source, ranging from 0 to around 500 mg/l (Figure 27). Probably due to the source term input at a stationary position and overestimation of the IM1 fraction.

For accuracy comparison the satellite image of 01/01/12 is used, because this image captured four active TSHD vessel. The differences between the PD-model and SB-model that were observed: RMSE was +17.3 mg/l, BIAS was +3.85 mg/l, R^2 was -0.097, and the plume extent was +18.4 % greater in the model compared to satellite observations (8.8% plume extent). These metrics highlight significant discrepancies between the model predictions and observed data, indicating a substantial level of uncertainty. The observed differences in RMSE and BIAS underscore systematic variances between predicted and observed values. While the model captures general trends, specific concentrations vary significantly (more plots and information in Appendix D). In conclusion, the PD-model is worse than the SB-model in accuracy, magnitude and average difference. Therefore the satellite images help improve the model plume predictions.

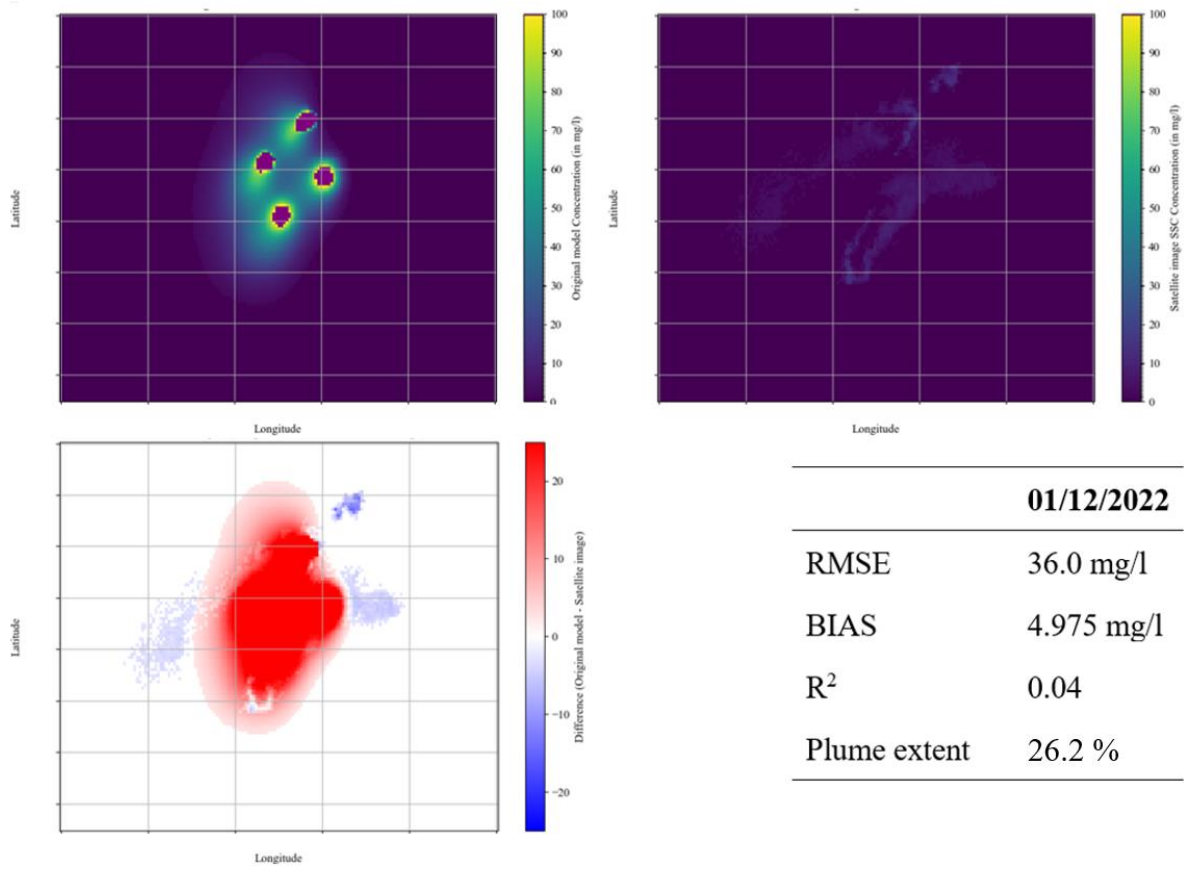

	01/12/2022
RMSE	36.0 mg/l
BIAS	4.975 mg/l
R^2	0.04
Plume extent	26.2 %

Figure 27: PD-model plume of the top left and the satellite image of 01/12/2022 on the top right. The bottom left image shows the difference between the PD-model and the satellite image TSS concentrations. On the bottom right are the analyses parameters added for the plume extent percentage relative to the Area of rectangle of the satellite image and the RMSE, BIAS (in mg/l) and R^2.

6| DISCUSSION

In this discussion, the results will be discussed in comparison to the initial objectives, focusing on the importance of the research, the challenges faced, and defining potential improvements to the current modelling of TSS concentrations. The primary objective of this study was to investigate the extent to which model assumptions regarding sediment dispersion parameters could be improved using plume extents derived from satellite imagery.

6.1 Sediment transport model parameters

The sediment transport model is challenging due to several factors. Firstly, the hydrodynamic forcing mechanisms, such as currents, tides and wind, have a significant impact on the behaviour of the sediment plume. Traditional models often struggle to accurately simulate these forces, leading to discrepancies in predictions(Smith et al., 2019). This phenomenon was also observed in the sediment transport SB-model. The dispersion and direction of the sediment plume differed from that of the satellite image TSS plume. To illustrate, the satellite image of 01/12/2022 depicts TSHD 5 with a plume that exhibits a greater westward movement and a relatively low plume concentration when compared to the sediment transport SB-model (Figure 23). The SB-model exhibited a more southerly movement and a larger plume extent. The discrepancies observed in the hydrodynamic model have influenced the direction and dispersion of the sediment plume. The question is to what extent this has affected the conclusions.

The hydrodynamic model had an R^2 of 0.32 with an RMSE of 0.08 m/s and a slightly positive bias (0.003 m/s). The hydrodynamic model would provide better estimates of water flow velocities, directions and turbulence. The improved accuracy translates directly into more reliable inputs to the sediment transport model. This leads to more accurate predictions of sediment transport rates and deposition patterns. Improving the R^2 would mean a better proportion of the variance in the TSS concentrations, leading to more accurate predictions of sediment transport rates and deposition patterns. Reducing the RMSE would reduce the overall prediction errors leading to better estimates of current velocities and removing bias would remove systematic errors leading to balanced and unbiased sediment transport predictions.

Incorporating additional hydrodynamic forcing mechanisms, such as river discharge from the Pasig River, could enhance the model's precision making the sediment transport model more reliable.

In addition to the hydrodynamic model, there are also many uncertainties in the sediment transport model. The largest uncertainties are in the fall velocity, source term and dispersion factor. For these parameters there is room for improvement. The study by J. Boersma, (2023) concluded that the sensitivity of the model was observed with respect to the source term and the fall velocity, but not with respect to the dispersion coefficient, which is different from what was observed in this study. The difference in results is probably due to the hydrodynamic forcing mechanisms. The plume modelled by J. Boersma was a stationary plume in an enclosed water body without tidal currents, while the model for Manila Bay included a moving source term in a semi-enclosed water body and had tidal currents.

For the fall velocity deposition, the results showed that this value was correctly estimated for the PD model. Only the fall velocity can vary over the course of dredging operations due to changes in particle size, water turbulence and sediment composition. This affects sediment deposition rates and the overall distribution and accumulation of dredged material (van Maren *et al.*, 2015). In order to improve the rate of fall, sediment fractions are used in the model, which offers practical advantages in terms of different rates of fall. However, this also introduces a new uncertainty in the composition of the fines. Using only one IM1 fraction eliminated the uncertainty in the fines composition, but had a higher uncertainty compared to using 2 IM fractions. Normally, when 2 IM fractions are used in the model, the IM1 fraction contains 66% of the fines and IM2 contains 33%. However, this research concludes that to add a realistic fall velocity (close to the Stokes formula result) the fractions should be split into IM1 33% and IM2 66%.

The source term was improved by using log files when available and by looking at the satellite images. It was concluded that the source term was best when set to the 80 % exceedance peak overflow source term with the empirical derived parameters at the top of the Becker (2015) derived range. For each vessel and satellite image differing source terms were used. A vessel does not dredge and overflow the same amount of time each dredging cycle. Next to the

differing dredging cycle, the amount of fines, the volume dredged and overflow position change making it difficult to estimate the correct source term.

To improve the source term, these factors should be taken into account, particularly the amount of fines and the starting point and position of the overflow. The overflow changed during the dredging cycle due to factors such as release position, frequency and the presence of a propeller. The propeller affects the advection and diffusion characteristics of the plume. Rear overflow, high release and the presence of a propeller result in more dispersed and diffused sediment plumes, whereas forward overflow, low release frequency and the absence of a propeller result in more stable concentrations (Chen *et al.*, 2022). By analysing the log files, the uncertainty of the source term can be minimised. Extraction of dredge time, overflow start time and position.

Therefore, it is possible to plan dredging cycles, but it is difficult to adhere to such a plan during project implementation, making source term predictions difficult. This is probably why the PD-model source term (which also used the P80 values) was overly conservative compared to the SB-model. The model was based on a repeating pattern with the same source term for each dredging cycle and a stationary position. In reality, the source terms are different for each dredging cycle.

The dispersion factor controls the horizontal dispersion of the sediments and is typically set to 1 m^2/s for the PD-model. However, in the sensitivity analysis of the SB model, the plume prediction was better with a dispersion factor of 3 m^2/s relative to the satellite image concentration than with a dispersion factor of 1 m^2/s.This may be due to the input of a moving source term along the AIS ship track compared to the use of a single and constant source term, as the dispersion is increased compared to the PD-model and the study by J. Boersma (2023). The source term is added with a time interval of 1 minute along the AIS ship track, while the PD-model and J. Boersma, (2023) had a stationary input. This is switched on and off according to the dredging cycle.

In conclusion, based on these experiences there was a different approach for the sediment transport model in Project and Design phase relative to the executable phase. By updating the SB-model in the executable phase with satellite images the source term, fall velocity and

dispersion factor were improved (Table 27). These values could be used in the Project and design phase to improve the source term and fall velocity. The dispersion factor will be more difficult due to the difference in stationary and moving vessels. The satellite imagery can help refine the models, leading to better-informed decision-making.

Table 27: PD-model vs SB-model vs Satellite image data: TSS concentrations (in mg/l) along the AIS-vessel track 1, 3 and 4 km from the source and the fall velocity, source term and dispersion coefficient values are displayed.

	PD-model	01/12 SB	01/12 Sat	01/22 SB	01/22 Sat.	03/28 SB	03/28 Sat.
1.0 km	>100	7.3	2.5	5.2	1.6	39.4	14.3
3.0 km	90	4.6	4.2	2.4	2.4	11.5	8.4
4.0 km	70	2.9	3.1	6.6	1.3	13.5	1.6
Source term (g/s)	6888 3444 5333 2667	670 1340 4100 8200		515 1030 3205 6410		560 1120 3480 6960	
Dispersion coefficient (m^2/s)	1	3	3	3	3	3	3
Fall velocity IM1 (m/d)	8.64	8.64	8.64	8.64	8.64	8.64	8.64
Fall velocity IM2 (m/d)	138.24	138.24	138.24	138.24	138.24	138.24	138.24

6.2 Degree of accuracy PD-model vs SB-model

The accuracy of the PD-model and of the improved SB-model are analysed by calculating the average RMSE, bias (in mg/l), adjusted R^2 and plume extent % values (Table 32) against the satellite image TSS concentration values. The SB-model has a significantly lower RMSE compared to the PD-model. This indicates that the SB-model predictions are much closer to the observed values. The R^2 is higher for the SB-model, indicating that the SB-model explains more variance in the data and therefore fits the data better than the PD-model. The bias is lower for the SB, indicating that the SB-model has predictions that are on average closer to the

satellite image TSS values. In conclusion the satellite imagery can improve the PD-model. The PD-model had a smaller RMSE (by 17.3 mg/l), bias (3.85 mg/l smaller), R^2 (0.1 higher), and the plume extent with 18.4 % greater in the model compared to satellite observations (8.8% plume extent) (Table 28). Therefore, the SB-model showed better performance in terms of unbiased predictions and plume extents.

Table 28: Average RMSE, R2, BIAS of the TSS concentration (in mg/l) PD-model and SB-model vs satellite image TSS concentrations.

Date	Metric	PD-Model	SB-Model
Average	RMSE (in mg/l)	36.13	2.47
	Adjusted R^2 (in mg/l)	0.03	0.13
	BIAS	5.03	0.30
	Plume extent %	87.1	17.7

From these results it can be concluded that the PD-model can be improved by almost 18 times in the mean error and 15 times the mean deviation in terms of concentrations and almost 5 times in terms of plume extents. The SB-model could be improved in terms of the implementation of the hydrodynamic model calibration source term. If the hydrodynamic model is more accurate, then the plume will be more accurate. However, a hydrodynamic model does not take into account wind circulation in the bay, which could affect the top layer. Further details on the differences between the hydrodynamic and sediment transport model settings can be found in Appendix C.

6.3 Feedback loop

The hydrodynamic and sediment transport models have been validated against in situ measurements and satellite imagery. The performance of these models was assessed and revealed several key findings and discrepancies. These findings and discrepancies require the implementation of a feedback loop to improve model accuracy and reliability.

The main objective of this research was to improve sediment plume prediction models using satellite imagery to better capture the plume and improve the models accuracy. RMSE, R^2 and BIAS can be used as benchmarks for the evaluation.

Regular and comprehensive data are essential for a feedback loop, but for this research, the amount of usable satellite imagery and log files was limited. Therefore data for the sediment transport model should be collected from a variety of sources, including:

- In-situ measurements, which involve capturing the tidal amplitudes, current velocities, current directions, wind patterns, and sediment composition.
- Satellite imagery: The periodic acquisition of satellite images spread throughout the year, including clear sediment-dredging plumes.
- Log files of the dredging vessels, in order to capture the dredging cycles of the vessels at the specific location.

With regard to the data analysis phase, the comparison of the model outputs with observed data should involve the following:

- Trend analysis: Evaluate the consistency of the tidal, current, and wind patterns across different monitoring stations near the model area.
- Discrepancy identification: Identify why and where the model differs from the satellite and observed data.
- Statistical evaluation: Use RMSE R^2, bias, maximum concentration, AIS datapoint profiles, and plume extents to measure and qualify the model's performance.

The project team could hold feedback sessions based on gathered data. In these sessions the data can be discussed regarding the sediment plume behaviour, the observed satellite imagery and the potential improvements.

The project team can hold a feedback session based on the gathered data, discussing the behaviour of the sediment plume model, observed satellite imagery, potential improvements, and actionable steps to refine the models and project. By using multiple satellite images and information from the feedback session previous model scenarios can be improved in the source

term, fall velocity and dispersion factor. When changing the parameters it is recommended to thoroughly document the changes and why in order to keep track.

Following the model's implementation, its performance must be monitored throughout the project execution phase, with the goal of assessing both its impact and the potential for iterative refinement in light of any new data and feedback. It is essential to adopt an iterative approach to model refinement. The loop will be stopped when the project comes to an end.

Upon completion of the feedback cycle and end of the project, a comprehensive review should be done to evaluate the effectiveness of the implemented changes and identify areas of further improvement, documenting the lessons learned and sharing findings with the organization to improve overall project outcomes.

Based on the research results, specific feedback is that the model should better reflect hydrodynamic forces by improving the wind, current, and tide parameters using data from measurements taken near the borrow area. It is recommended that the sediment transport model be modified to more accurately account for overflow variability during dredging operations, thereby improving the accuracy of near- and far-field predictions.

The sensitivity analysis highlights the significance of grid size, Courant number, timestep, dispersion factor, load, and IM1 and IM2 distribution on model accuracy. Adjustments to these parameters should be made in a manner that balances calculation time and predictive accuracy.

7| CONCLUSIONS AND RECOMMENDATIONS

7.1 Conclusion

Satellite imagery can be a valuable tool for refining assumptions about sediment dispersion parameters, particularly plume extent, which can be used to improve model accuracy. The imagery allows real-time verification and modification of the SB-model's upper layer sediment plume. The SB-model showed improved performance over the PD-model with a lower RMSE, higher R^2, lower bias and better plume extent. This indicated closer and more accurate predictions to the satellite image TSS concentration values. This is partly due to the available log files and AIS-data, but mostly due to the satellite image TSS concentration values. The satellite imagery improves the model prediction by calibrating the performance of the model against the satellite imagery TSS concentrations in a specified area. Changing the source term, fall velocity and dispersion factor to match the model as best as possible to the satellite image.

The sediment transport PD-model was based on a number of assumptions and estimates, particularly in relation to the source term, dispersion factor and fall velocity. By incorporating the satellite images and a more realistic dredging cycle it was managed to calibrate the model parameters. Using the satellite image TSS concentration values for the calibration verifying and analysing the model output.

The source term values were improved by adjusting the dredging cycle according to the log files and satellite image TSS concentration values. However, the position of the plume changes during the operation, resulting in a variable plume which presents a challenge to the calculation of the peak source term. From the calibration is concluded that the dispersion factor depends on both the sediment composition and the movements of the vessel. The PD-model uses a dispersion factor of 1 m^2/s, and the SB-model uses 3 m^2/s. This is probably because the PD-model uses a stationary source term and the SB-model uses a moving source term. The PD-model predicts the fall velocity accurately, but the IM fraction distribution is different. The PD-model uses IM1 66% and IM2 33% while the SB-model uses IM1 33% and IM2 66%. When the PD-model's IM fractions are applied to the SB-model, the fall velocity must be

increased to unrealistic values, whereas with the SB-model's distributions the fall velocity can remain the same.

The accuracy of the PD-model was low in terms of concentration values compared to the SB-model. The PD-model has a RMSE of 36.1 mg/l, no correlation and BIAS of 5.01 mg/l. The SB-model has a slightly improved RMSE of 2.4 mg/l, R^2 of 0.13 and a BIAS of 3.0 mg/l. While the satellite image has proven to be useful for refining the model parameters, the low correlation of the PD-model indicates there is still room for improvement. By the use of more satellite imagery, log files and a feedback loop for continuous refinement of the model, parameters could contribute to a more accurate and reliable sediment transport model in the long run. Another improvement could be more complex hydrodynamic forcing mechanisms in the hydrodynamic model which can help improve the accuracy of the plume behaviour in the sediment transport model. In addition, it is important to consider the significant influence of changing the grid size, time step, dispersion factor, loading and IM1 and IM2 fraction distributions.

In conclusion, satellite imagery can help to refine model assumptions. However, it would be beneficial to have access to more satellite imagery TSS concentration data and to compare more models with satellite images that have a distinguishable plume with the same vessel.

7.2 Recommendations

Each model is characterized by a distinct set of uncertainties. However, it is possible to mitigate these uncertainties by using in-situ data to improve the hydrodynamic model and satellite imagery to improve the sediment transport model. When the hydrodynamic model is not performing correctly, the sediment transport model will exhibit even greater uncertainty. The results of this research illustrate the potential of the utilisation of sediment transport SB-models in a feedback loop in the executable phase. With the satellite imagery and log files, sediment transport models can be logged more accurately at the top layer.

To enhance the data collection process and improve model accuracy, several recommendations stand out:

- Expand the amount of satellite image TSS data by adding multiple satellite sources, not only Sentinel-2 data.
- Conduct detailed sensitivity analysis on multiple satellite image dates with the same vessel, clear plume and available log files.
- Balance computational efficiency and accuracy when adjusting model parameters in the hydrodynamic and sediment transport model.
- Use an iterative process and update the information on the topic regularly to provide the best feedback loop and to ensure optimal data usage.

7.2.1 Improvements for the sediment transport model

Additionally, specific recommendations for improving the sediment transport model include:

- The examination of ship log files can provide valuable insight into the progression of the overflow, given the inherent variability in the position of the overflow during the dredging process.
- The dispersion coefficient exerts a significant influence on the size of the plume extents observed in the top layer. An increase in dispersion results in a larger plume along the entire vessel track, accompanied by a reduction in concentration.
- It is recommended that the sediment fractions in the top layer be set to IM1 33% and IM2 66%, with a P80 overflow peak source term, to achieve the most accurate estimation of the top layer sediment plume. When the fall velocity is set to a value considerably higher than that required to create the correct plume, the result is a representation that does not reflect reality.
- The hydrodynamic model necessitates a spin-up time of two days, whereas the sediment transport model can be simulated in approximately six hours. This is sufficient to observe the plumes in a satellite image. The plumes generated by dredging operations prior to the six-hour mark have already settled and are not visible in the satellite image.
- To achieve a more precise estimation of the vessel source terms, a sensitivity analysis could be conducted using multiple satellite images with distinguishable plumes and the same vessel.

By applying these recommendations, the sediment transport plume model accuracy can be improved, leading to more reliable and better-managed operations.

7.2.2 Recommendations for future research

For future research, the following questions are recommended:

- How much does a varying source term per overflow position affect the eventual sediment plume?
- What are the implications of modifying the source term in the upper layer for the subsequent layers?
- To what extent can the iterative process of the feedback loop, utilizing a greater number of satellite images, enhance the accuracy of the sediment transport parameters?
- What is the effect of an adjustable overflow source term in accordance with the overflow position on the sediment transport SB-model plume?

By implementing these recommendations and addressing the outlined research questions, the project team can significantly enhance the data collection process and improve the accuracy and reliability of sediment plume prediction models. This holistic approach will contribute to better-informed decision-making and more effective management of sediment transport and dredging operations.

8| REFERENCES

AbuShanab, M. (2022) ‘Remote sensing of sediment plumes using Satellite Image Research.’ *MSc 2 graduation internship*. University TU Delft, pp. 1-25. Accessed: 03 September 2024.

Balduzzi, F., Bianchini, A., Ferrara, G. and Ferrari, L. (2016) ‘Dimensionless numbers for the assessment of mesh and timestep requirements in CFD simulations of Darrieus wind turbines’, *Energy*, 97, pp. 246–261. Available at: https://doi.org/10.1016/j.energy.2015.12.111 (Accessed: 07 January 2024).

Barnes, B.B., Hu, C., Kovach, C. and Silverstein, R.N. (2015) ‘Sediment plumes induced by the Port of Miami dredging: Analysis and interpretation using Landsat and MODIS data’, *Remote Sensing of Environment*, 170, pp. 328–339. Available at: https://doi.org/10.1016/j.rse.2015.09.023 (Accessed: 04 January 2024).

Becker, J., Van Eekelen, E., Van Ledden, M., Suzuki, T. and Winterwerp, H. (2015) ‘Estimating source terms for far-field dredge plume modelling’, *Journal of Environmental Management*, 149, pp. 282–293. Available at: https://doi.org/10.1016/j.jenvman.2014.10.022 (Accessed : 03 August 2024).

Blaas, M., Dong, C., Marchesiello, P., McWilliams, J.C. and Stolzenbach, K.D. (2007) ‘Sediment-transport modeling on Southern Californian shelves: A ROMS case study’, *Continental Shelf Research*, 27(6), pp. 832–853. Available at: https://doi.org/10.1016/j.csr.2006.12.003 (Accessed: 15 January 2024).

Boersma, J.M. (2023) ‘*From Space to Sea: An Exploratory Study on Parameter Estimation for Sediment Plume Models using Remote Sensing Data*’. University TU Delft, pp. 1-66. Accessed: 20 September 2024.

Boskalis (2024) *Boskalis Company profile*. Available at: https://boskalis.com/ (Accessed: 10 January 2024).

Caballero, I., Navarro, G. and Ruiz, J. (2018) ‘Multi-platform assessment of turbidity plumes during dredging operations in a major estuarine system’, *International Journal of Applied*

Earth Observation and Geoinformation, 68, pp. 31–41. Available at: https://doi.org/10.1016/j.jag.2018.01.014 (Accessed: 19 January 2024).

Chen, Q.-Y., Liu, M., Zhang, W., and Wang, Y.-H. (2022) "Study on the dynamic characteristics of the overflow advection and diffusion of trailing suction hopper dredgers based on CFD," *Ocean Engineering*, 252. Available at: https://doi.org/10.1016/j.oceaneng.2022.111263 (Accessed: 07 September 2024).

Deltares (2024a) *Delft3D fM Suite Simulation software for safe, sustainable and future deltas User Manual D-Flow Flexible Mesh*. Available at: https://oss.deltares.nl/web/delft3d/manuals (Accessed: 25 April 2024).

Deltares (2024b) *Water Quality Water quality and aquatic ecology modelling suite User Manual Water Quality and Aquatic Ecology*. Available at: https://oss.deltares.nl/web/delft3d/manuals (Accessed: 30 June 2024).

DHI (2022) *MetOcean wind data*. Available at: https://www.dhigroup.com/technologies/metocean-data-portal (Accessed: 2 June 2024).

Dogliotti, A.I., Ruddick, K.G., Nechad, B., Doxaran, D. and Knaeps, E. (2015) 'A single algorithm to retrieve turbidity from remotely-sensed data in all coastal and estuarine waters', *Remote Sensing of Environment*, 156, pp. 157–168. Available at: https://doi.org/10.1016/j.rse.2014.09.020 (Accessed: 15 January 2024).

Erftemeijer, P.L.A., Riegl, B., Hoeksema, B.W. and Todd, P.A. (2012) 'Environmental impacts of dredging and other sediment disturbances on corals: A review', *Marine Pollution Bulletin*, 64(9), pp. 1737–1765. Available at: https://doi.org/10.1016/j.marpolbul.2012.05.008 (Accessed: 15 January 2024).

Giavarina, D. (2015) 'Understanding Bland Altman analysis', *BiocheProject 1Biochemia Medica*, 25(2), pp. 141–151. Available at: https://doi.org/10.11613/BM.2015.015 (Accessed: 20 January 2024).

Hayes, M.C., Jones, A., Smith, R. and Brown, L. (2022) ‘Estimating dredge-induced turbidity using drone imagery’. Available at: https://doi.org/10.20944/preprints202201.0424.v1 (Accessed: 17 January 2024).

Hodson, T.O. (2022) ‘Root-mean-square error (RMSE) or mean absolute error (MAE): when to use them or not’, *Geoscientific Model Development*. Copernicus GmbH, pp. 5481–5487. Available at: https://doi.org/10.5194/gmd-15-5481-2022 (Accessed: 19 January 2024).

IADC (2023) ‘Dredging in Figures’. Available at: https://www.iadc-dredging.com/news/dredging-in-figures-2022-published/ (Accessed: 14 January 2024).

Islam, M.A. (2007) ‘Evaluation of satellite remote sensing for operational monitoring of sediment plumes produced by dredging at Hay Point, Queensland, Australia’, *Journal of Applied Remote Sensing*, 1(1), p. 011506. Available at: https://doi.org/10.1117/1.2834768 (Accessed: 03 January 2024).

Kim, N.H., Lee, S.H., Kim, H.C., and Park, J.M. (2018) ‘Effects of seasonal variations on sediment-plume streaks from dredging operations’, *Marine Pollution Bulletin*, 129(1), pp. 26–34. Available at: https://doi.org/10.1016/j.marpolbul.2018.02.014 (Accessed: 16 February 2024).

Laboyrie, P., Van Koningsveld, M., Aarninkhof, S., and Van Gelder, P. (2018) ‘Dredging for Sustainable Infrastructure’, in. CEDA/IADC, p. 336 (Accessed: 17 March 2024).

Leo van Rijn (2019) *Turbidity due to Dredging and Dumping of Sediments*. Available at: www.leovanrijn-sediment.com (Accessed: 12 March 2024).

Luis, J.F. (2007) ‘Mirone: A multi-purpose tool for exploring grid data’, *Computers and Geosciences*, 33(1), pp. 31–41. Available at: https://doi.org/10.1016/j.cageo.2006.05.005 (Accessed: 25 Juli 2024).

van Maren, D.S., Van Kessel, T., Cronin, K., and Sittoni, L. (2015) “The impact of channel deepening and dredging on estuarine sediment concentration,” *Continental Shelf Research*, 95, pp. 1–14. Available at: https://doi.org/10.1016/j.csr.2014.12.010 (Accessed: 15 September 2024).

Mendoza, F.P., Marques, W.C., Fernandes, E.H., and Moller, O.O. (2018) 'Circulation during storms and dynamics of suspended matter in a sheltered coastal area', *Remote Sensing*, 10(4). Available at: https://doi.org/10.3390/rs10040602 (Accessed: 02 January 2024).

PennState Eberly College of Science (2018) 'The Coefficient of Determination, r-squared'. Available at: https://online.stat.psu.edu/stat462/node/95/ (Accessed: 02 July 2024).

Peters, S., Hommersom, A. and Laanen, M. (2021) *Digitale monitoring baggerpluimen markerwadden*. Accessed: 17 August 2024.

Peters, S., Spais, L. and Hommersom, A. (2022) *Validation of satellite based products with in situ data in Manila Bay*. Accessed: 18 Augustus 2024

'QGIS Geographic Information System.' (2024). Open Source Geospatial Foundation Project. Accessed: 25 Juli 2024.

Raunek (2023) 'What is Dredging – History, Importance And Effects'. Available at: https://www.marineinsight.com/guidelines/what-is-dredging/ (Accessed: 08 January 2024).

van Rijn (2007) *Simple general formulae for sand transport in rivers, estuaries and coastal waters.* Available at: www.leovanrijn-sediment.com (Accessed: 18 June 2024).

Rijper, H. (2021) *Project 1 Detailed Assessment of Dredging-Induced Turbidity-Draft Borrow Area □ CODE 4: accepted for information only*. Accessed: 17 September 2024.

Schmunk Robert (2024) 'Panoply'. NASA. Available at: https://www.giss.nasa.gov/tools/panoply/ (Accessed: 17 April 2024).

Seraphin, D.K. (2024) *Tide Patterns and Currents*. Available at: https://manoa.hawaii.edu/exploringourfluidearth/physical/tides/tide-patterns-and-currents (Accessed: 15 June 2024).

Smith, L., Sandwell, D., and Mellors, R. (2019) 'Evidence of Environmental Changes Caused by Chinese Island-Building', *Scientific Reports*, 9(1). Available at: https://doi.org/10.1038/s41598-019-41659-3 (Accessed: 17 June 2024).

Son, S.H., Wang, M., and Shon, Z.H. (2014) 'Characterization of spatial and temporal variation of suspended sediments in the Yellow and East China Seas using satellite ocean color data', *GIScience and Remote Sensing*, 51(2), pp. 212–226. Available at: https://doi.org/10.1080/15481603.2014.895580 (Accessed: 07 February 2024).

Spearman, J., Taylor, J., Crossouard, N., Cooper, R., Turnbull, M., and Manning, A.J. (2020) 'Measurement and modelling of deep sea sediment plumes and implications for deep sea mining', *Scientific Reports*, 10(1). Available at: https://doi.org/10.1038/s41598-020-61837-y (25 December 2023).

Sta. Maria, E.J., Siringan, F.P., and Maeda, Y. (2009) 'Estimating sediment accumulation rates in Manila Bay, a marine pollution hot spot in the Seas of East Asia', *Marine Pollution Bulletin*, 59(4–7), pp. 164–174. Available at: https://doi.org/10.1016/j.marpolbul.2009.04.017 (Accessed: 17 September 2024).

Sun, C., Branson, P. and Mills, D. (2020) *WAMSI Dredging Science Node Guideline on dredge plume modelling for environmental impact assessment*. (Accessed: 07 January 2024).

Tuinhof, T. (2014) 'Modelling far-field dredge plume dispersion', *Master's thesis*, TU Delft University. Accessed: 14 April 2024.

United Nations (2015) 'Transforming our world: The 2030 agenda for sustainable development'. Available at: https://sdgs.un.org/2030agenda (Accessed: 17 January 2024).

Wenger, A.S., Harvey, E., Wilson, S., Rawson, C., Newman, S.J., Clarke, D., Saunders, B.J., Browne, N., Travers, M.J., Jones, R., and Evans, R.D. (2017) 'A critical analysis of the direct effects of dredging on fish', *Fish and Fisheries*, 18(5), pp. 967–985. Available at: https://doi.org/10.1111/faf.12218 (Accessed: 13 January 2024).

Willemsen, M.P.J. (2022) 'An Analysis of Trailing Suction Hopper Dredger Dredge Plume Development and the Use of Suspended Sediment Source Terms A numerical simulation study MSc Hydraulic Engineering An Analysis of Trailing Suction Hopper Dredger Dredge Plume Development and the Use of Suspended Sediment Source Terms A numerical simulation study', *Master's thesis*, TU Delft university. Accessed: 15 April 2023

de Wit, L. (2015) ‘3D CFD modelling of overflow dredging plumes’, *Doctoral dissertation*, TU Delft University. Accessed: 15 March 2024.

de Wit, L., Bliek, B. and van Rhee, C. (2020) *‘Can surface turbidity plume generation near a trailing suction hopper dredger be predicted?’* Available at: https://www.iadc-dredging.com/article/turbidity-plume-generation-hopper-dredger/ (Accessed: 17 January 2024).

Zulueta, V.J.M. (2023) ‘Water quality analysis on neritic zones of Manila Bay Dolomite beach and its contribution to ecosystem services’, *Master’s thesis*, University of the Philippines Open University. Accessed: 17 September 2024.

9| APPENDICES

Appendix A	Hydrodynamic model sensitivity analysis
Appendix B	Satellite imagery
Appendix C	Sediment transport SB-model
Appendix D	PD-model
Appendix E	Python scripts
Appendix F	Area extents